Received: 25 May 2023 | Revised: 16 November 2023 | Accepted: 22 December 2023

DOI: 10.1002/qj.4667

Quarterly Journal of the Royal Meteorological Society RMetS

RESEARCH ARTICLE

Impact of the Madden–Julian oscillation and equatorial waves on tracked mesoscale convective systems over southeast Asia

Julia Crook[1] | **Fran Morris**[1] | **Rory Gordon John Fitzpatrick**[1] | **Simon C. Peatman**[1] | **Juliane Schwendike**[1] | **Thorwald H. Stein**[2] | **Cathryn E. Birch**[1] | **Sam Hardy**[1] | **Gui-Ying Yang**[2,3]

[1]Institute for Climate and Atmospheric Science, School of Earth and Environment, University of Leeds, Leeds, UK

[2]Department of Meteorology, University of Reading, Reading, UK

[3]National Centre for Atmospheric Science, University of Reading, Reading, UK

Correspondence
Julia Crook, Institute for Climate and Atmospheric Science, School of Earth and Environment, University of Leeds, Leeds, UK.
Email: j.a.crook@leeds.ac.uk

Funding information
Natural Environment Research Council, Grant/Award Number: NE/R016739/1; WCSSP Southeast Asia Newton Fund

Abstract

Southeast Asia is a region dominated by high-impact weather, but numerical weather prediction here is a challenge owing to the complex orography and interactions between small- and large-scale phenomena. Localised mesoscale convective systems (MCSs) can produce intense precipitation. Here, we track MCSs over a 5-year period in Himawari satellite data, characterise the distribution of MCSs in the region, and investigate how they are modulated by the Madden–Julian oscillation (MJO) and equatorial waves. Between 10°S and 10°N in southeast Asia, MCSs account for 45–70% of the precipitation during boreal extended winter (November–April). Over most of the region, the fractional MCS contribution to rainfall is higher than average on days with extreme rainfall (>55%). Long-lived (>12 hr) MCSs contribute disproportionately, providing 85% of the rainfall despite comprising only 34% of all MCSs. Variability in MCS rainfall accounts for >50% of the total rainfall variability during an MJO cycle, mostly due to larger numbers of MCSs in convectively active MJO phases. Variations in MCS size and mean rain rate due to shifts in the stratiform proportion provide compensating effects. In the west of the region, a shift to faster moving MCSs in active MJO phases and slower moving MCSs in inactive phases resulted in fast-moving MCSs having the greatest impact on the MJO-associated variability. Variability is larger in the west than in the east. Equatorial Kelvin waves modulate MCS rainfall, with MCSs accounting for 20–50% of local rainfall anomalies. This variability is again enhanced in the west. By contrast, rainfall anomalies due to westward-propagating mixed Rossby–gravity waves and Rossby-1 waves are dominated by tropical-cyclone-related rainfall. Skill at local scales may be extracted from forecasts of subseasonal drivers such as the MJO and Kelvin waves, by understanding how these modulate the number and characteristics of MCSs.

KEYWORDS

equatorial waves, Madden–Julian oscillation, mesoscale convective systems, rainfall variability, southeast Asia

1 | INTRODUCTION

Southeast Asia (Figure 1) is a region of particularly warm sea-surface temperatures, which, combined with its equatorial location and the position of the intertropical convergence zone, gives rise to large-scale ascent and an unstable vertical profile. This results in intense convection, heavy rain, and large amounts of latent heat release, which impacts the global climate system, acting as an atmospheric "boiler box" (e.g., Neale & Slingo, 2003; Ramage, 1968; Simpson *et al.*, 1993). The region is prone to flooding and landslides due to frequent high-impact weather (Adhikari *et al.*, 2010; Ferrett *et al.*, 2020), and communities in the region are reliant on accurate forecasting of high-impact weather events to prepare for and mitigate risks. Tropical cyclones and depressions are associated with some of the more high-profile high-impact weather events, given the high probability of flooding from precipitation or storm surges, and wind damage associated with these events. However, more localised mesoscale convective systems (MCSs), which can also produce intense precipitation, also have the potential to cause loss of property or life over the region. Southeast Asia is of interest from a meteorological research perspective given the complex topography of the region, as well as the documented influence of large-scale circulation features on local weather variability (e.g., Peatman *et al.*, 2021). Furthering our understanding of the connection between heavy precipitation and both the Madden–Julian oscillation (MJO) and equatorial waves is crucial for both forecasting and improving climate models (Da Silva & Matthews, 2021; Huang *et al.*, 2012; Li & Stechmann, 2020; Yang *et al.*, 2009; Ying & Zhang, 2017).

MCSs are convective storms that grow to hundreds of kilometres in size and can last for more than a day (Houze, 2004). They have convective cores spanning ~10–100 km in the horizontal, with heavy rainfall embedded in a stratiform anvil cloud and lighter precipitation that extends over a region 100–1,000 km in length (Houze, 2018; Roca & Ramanathan, 2000). They produce a larger volume of rainfall per storm than other deep convective systems and have a large proportion of stratiform rain. This stratiform rain leads to a top-heavy latent heating profile. The combined upper level heating from all MCSs results in a strong upper level circulation response that has a large impact on the global circulation, and therefore Earth's energy and hydrological cycle (Houze, 1997; Schumacher & Houze, 2003). MCSs produce more than half of the annual rainfall in the Tropics (Yuan & Houze, 2010), and in certain seasons over land regions the fraction can exceed 80% (Nesbitt *et al.*, 2006; Roca *et al.*, 2014). The longest lived MCSs preferentially occur over the subtropical oceans. Land MCSs have higher cloud tops associated with more intense convection, whereas oceanic MCSs have much higher overall rainfall production (Feng *et al.*, 2021). Roca *et al.* (2014) investigated the rainfall associated with MCSs of varying lifetime and propagation properties across the Tropics. They found systems lasting up to 24 hr account for 80% of MCS rain whereas those lasting <12 hr contribute ~25% of MCS rain. Systems that travel >250 km contribute ~60% of MCS rain, although those that travel <500 km contribute ~80% of MCS rain. Roca *et al.* (2014) analysed MCSs across much of the Tropics; however, they had no data available for the Maritime Continent region. Although much is now understood about the types of structure seen in MCSs, understanding the physical processes that organise MCSs and how they interact with larger scale atmospheric features is less well studied (Houze, 2018).

Satellite observations make it possible to study MCSs at the global scale via two distinct methods. The first method makes use of geostationary satellite data to track the evolution of MCSs based on their low cloud-top brightness temperature signatures in successive images (e.g., Huang *et al.*, 2018; Laing & Fritsch, 1997; Roca *et al.*, 2014). Fiolleau and Roca (2013) describe in detail some of the tracking methods that have been used. Tracking of MCSs allows understanding of these systems from a Lagrangian point of view, including lifetime and propagation aspects. Once cold cloud clusters have been identified and tracked using geostationary brightness temperature, further refinements are sometimes made to identify which of these meet the criteria of being an MCS; that is, that an MCS has both convective and stratiform rain covering an extensive area during its mature phase, and that it exists for a prolonged period. The second method is based on low-orbit satellite data, where advanced instruments (e.g., spaceborne radar and microwave radiometers) provide additional measurements of cloud and precipitation structures to characterise MCSs (Liu & Zipser, 2013; Nesbitt *et al.*, 2006; Yuan & Houze, 2010). This does not allow tracking but identifies cold cloud clusters that form during the mature phases of the MCS lifecycle and allows better estimation of their precipitation than using infrared alone. Combinations of the two methods allows for composite statistics of detailed MCS characteristics sampled along the MCS lifecycle (e.g., Bouniol *et al.*, 2021).

The MJO is the leading mode of intraseasonal variability across the Tropics (Madden & Julian, 1971, 1972, 1994). The MJO is an eastward-propagating disturbance located over the Indian and Pacific oceans that affects local convection and has planetary influences through the generation of equatorial Rossby and Kelvin wave disturbances (Hendon & Liebmann, 1994). The MJO has been observed to be a factor in determining the frequency, positioning, and intensity of high-impact weather

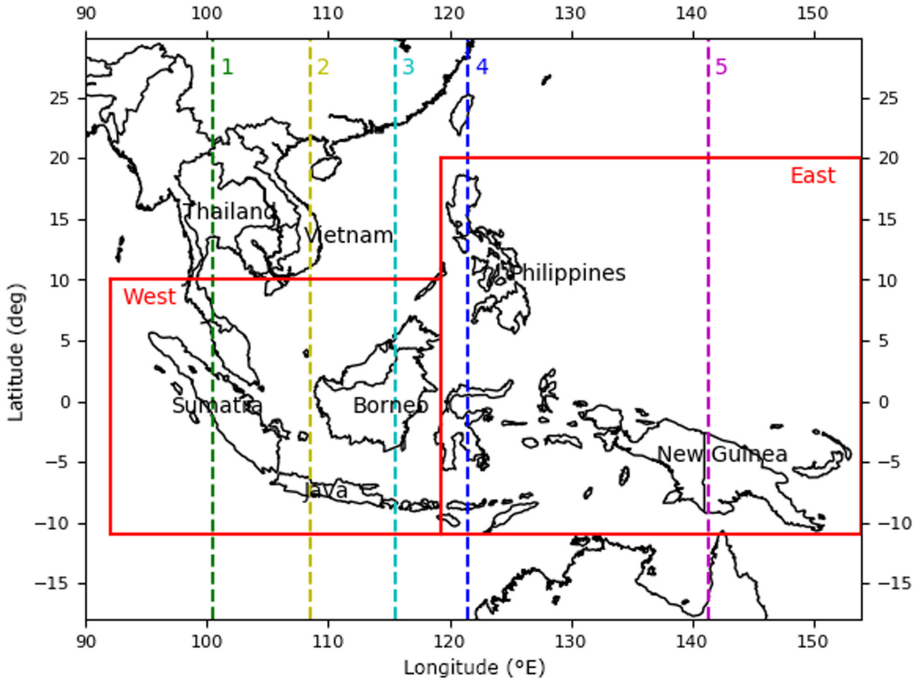

FIGURE 1 Map showing the analysis region, the two subregions (red boxes) analysed for the Madden–Julian oscillation, and longitudes (coloured dashed lines) analysed for equatorial waves (100.5°E relevant for weather in Sumatra and Thailand, 108.5°E for Java and Vietnam, 115.5°E for Indonesia, particularly Borneo, 121.5°E for Philippines and Sulawesi, and 141.5°E for New Guinea)

events, such as extreme rainfall across the Tropics (Jones *et al.*, 2004) in southwest Asia (Barlow *et al.*, 2005) and in southeast Asia (Da Silva & Matthews, 2021; Jeong *et al.*, 2008; Xavier *et al.*, 2014). In Indonesia, extreme precipitation events may be up to 70% more frequent in the convectively active phases of the MJO (Muhammad *et al.*, 2020). Intraseasonal variability of convective events tied to low-frequency eastward-propagating disturbances, such as active MJO events, has been observed to be greater during the boreal extended winter months November–April (NDJFMA; Wang & Rui, 1990), with similar variability in near-surface wind speeds amplified during December–February (Madden, 1986). The MJO moves further north during the boreal summer (Zhang & Dong, 2004). Accordingly, most analysis of the influence of the MJO on precipitation variability over southeast Asia is focused on boreal winter, or the northeast monsoon season (e.g., Birch *et al.*, 2016; Jeong *et al.*, 2008; Muhammad *et al.*, 2020; Peatman *et al.*, 2014; Xavier *et al.*, 2014).

Over southeast Asia, convection is enhanced during MJO phases 4 and 5, and it is suppressed during phases 8 and 1. A shift from shallow convection to deep convection during convectively active phases (4 and 5) of the MJO has been observed (e.g., Del Genio *et al.*, 2012; Stephens *et al.*, 2004), with the deep convection occurring due to moist midtropospheric conditions and strong low-level shear (Barnes & Houze, 2013). Fractional cloud coverage of MCSs and their contribution to rainfall were found to increase in convectively active MJO phases (Yuan & Houze, 2013). It has been suggested that, during the progression of an active MJO phase across the Maritime Continent, small individual MCSs become larger and deeper and aggregate to form MCS clusters with the proportion of stratiform rain increasing (Virtz & Houze, 2015; Zuluaga & Houze, 2013), thus mimicking the lifecycle of an individual MCS but over a much longer time-frame. Cheng *et al.* (2023) found that frequency, rain rates, and areas of MCSs were enhanced during the convectively active part of the MJO compared with climatology. The enhanced convection over land and coastal regions precedes that over the ocean by approximately one MJO phase (Birch *et al.*, 2016; Hagos *et al.*, 2016; Oh *et al.*, 2012; Peatman *et al.*, 2014). This earlier peak over land is associated with intensified surface heating and insolation, which in turn drives a strong land–sea breeze circulation (Birch *et al.*, 2016) and is particularly evident in regions where there is a strong diurnal cycle in rainfall; for example, over Sumatra, Borneo, and New Guinea (Peatman *et al.*, 2014). Part of this spatial variability is associated with an increase in longer lived systems over coastal regions when precipitation is favoured (Coppin *et al.*, 2020).

Equatorial waves have long been associated with deep convection and precipitation in the Tropics through observation (e.g., Chang, 1970; Kiladis *et al.*, 2009; Liebmann & Hendon, 1990; Takayabu, 1994; Wheeler & Kiladis, 1999; Yanai & Murakami, 1970; Yang *et al.*, 2007a, 2007b), and theoretical descriptions (see Gill, 1980) describe how they modulate atmospheric motions to create favourable environments for deep convection and precipitation. Furthering our understanding of the connection between such waves and extreme precipitation is crucial for

both forecasting and improving climate models (Huang *et al.*, 2012; Li & Stechmann, 2020; Yang *et al.*, 2009; Ying & Zhang, 2017). Convectively coupled waves are a major source of tropical rainfall variability (e.g., Lubis & Jacobi, 2015), a key element of the tropical circulation, and strongly influence tropical cyclogenesis (e.g., Dickinson & Molinari, 2002; Feng *et al.*, 2023; Frank & Roundy, 2006).

Various recent studies centred on southeast Asia have demonstrated that Kelvin waves, westward-propagating mixed Rossby–gravity (WMRG) waves, and equatorial Rossby waves can modulate wind fields (e.g., Peatman *et al.*, 2021) and synoptic weather systems (e.g., Hsu *et al.*, 2020) as well as rainfall over the Maritime Continent (Ferrett *et al.*, 2020). Both Baranowski *et al.* (2016) and Sakaeda *et al.* (2020) respectively show that the diurnal cycle is intensified by Kelvin waves and Rossby waves, the latter especially over the ocean. Chen *et al.* (2019) further emphasise the intensification of the diurnal cycle over land by Kelvin waves.

Ferrett *et al.* (2020) show that equatorial wave activity is linked to extreme rainfall in the region. Kelvin waves are strongly associated with extreme precipitation over Indonesia and Malaysia, whereas WMRG waves are associated with extreme rainfall over Malaysia and the Philippines, and Rossby waves largely only coincide with extreme rainfall over the Philippines. For example, over Java, Kelvin waves contribute most significantly to rainfall, increasing the probability of extreme rain events over land by up to 60% (Lubis & Respati, 2021). The $n = 1$ equatorial Rossby and WMRG waves are also shown to increase the probability by 45% and 40% respectively. Furthermore, Latos *et al.* (2021) estimate that the probability of flooding and extreme rain development over Sulawesi is doubled by the presence of Kelvin waves and Rossby waves, using a climatological analysis as well as examining a case study of flooding in January 2019. In particular, MCSs are a form of convection associated with convectively coupled equatorial waves (Kiladis *et al.*, 2009; Mapes *et al.*, 2006). The exact mechanisms through which MCSs couple to planetary-scale modes of variability such as equatorial waves and the MJO are uncertain. Further investigation into the relationship between MCS rainfall and equatorial waves and the MJO could help inform theories of MCS coupling.

In this study, we tracked MCSs over southeast Asia during a 5-year period using geostationary satellite data. In this article, we provide an overview of MCS characteristics during boreal extended winter (NDJFMA) and examine how MCS rainfall is modified in different phases of the MJO and equatorial waves. We show how the MJO phase affects different types of MCSs, classified according to how long they live and how fast they move, in terms of frequency, intensity, size, and location.

2 | DATA AND METHODOLOGY

2.1 | Observational data

In order to track MCSs, we used brightness temperature T_b from the Himawari-8 geostationary satellite (Bessho *et al.*, 2016). Infrared retrievals from Himawari channel 13 (10.4 μm) were used as they provide a long time series of the evolution of convective systems across southeast Asia at a high spatial and temporal resolution. The dataset has also been used in several multinational projects in recent years, including the Years of the Maritime Continent project (Yoneyama & Zhang, 2020). Owing to computational expense, data were coarse gridded to 4.4 km grid spacing with a temporal resolution of 1 hr before applying a storm-tracking algorithm (Section 2.2.2). These decisions are justified given previous studies that have accurately captured MCS behaviour at such spatial resolutions in the Tropics (Crook *et al.*, 2019; Feng *et al.*, 2021; Fitzpatrick *et al.*, 2020). We are unable to track storms on days when consecutive data are unavailable. Although data are available from June 2015 to May 2020, there are a particularly large number (169 times in 92 days) of consecutive missing times between June and August 2015, compared with 71 consecutive missing times in the remaining 1,735 days to May 2020. Therefore, our analysis period starts in September 2015.

Precipitation data were taken from the Integrated Multi-satellite Retrievals for the Global Precipitation Measurement (IMERG) mission dataset (Huffman *et al.*, 2020). The IMERG algorithm combines data from a network of partner satellites in the Global Precipitation Measurement constellation equipped with passive microwave and infrared sensors. The IMERG product is comparable to station data up to the 95th percentile over southeast Asia (Da Silva *et al.*, 2021). Data are available at 30-min intervals on a $0.1° \times 0.1°$ horizontal grid.

Wind data to analyse different environmental conditions in different MJO phases was taken from the fifth-generation European Centre for Medium-Range Weather Forecasts Reanalysis (ERA5) dataset (Hersbach *et al.*, 2020, 2023). The data used are six-hourly, on a 0.25° longitude–latitude grid with average grid spacing of 31 km in the Tropics and at 850, 500, and 200 hPa.

The real-time MJO multivariate indices were obtained from the Bureau of Meteorology real-time MJO tracking dataset (http://www.bom.gov.au/climate/mjo/graphics/rmm.74toRealtime.txt). We considered any day with MJO amplitude greater than or equal to 1.0 to be an "active" MJO day.

For equatorial waves, we used an existing dataset that applies the method outlined by Yang *et al.* (2003) to ERA5 data (Hersbach *et al.*, 2020, 2023). The technique

uses spatial projection onto theoretical horizontal wave-mode structures (the parabolic cylinder functions) at each pressure level (e.g., Gill, 1980). Before the projection, a broad-band spectral filter, with wave numbers $k = 2$–40 and period 2–30 days, is applied to separate eastward- and westward-moving waves. A full description of the dataset is available from Yang *et al.* (2023).

2.2 | Methods

2.2.1 | Region selection

Our analysis region spans 90–154°E, 18°S–30°N and covers all the major islands of the Maritime Continent and mainland southeast Asia, as well as a portion of the western Pacific Ocean (Figure 1). For some of the MJO analysis we show results for two subregions, West and East (Figure 1, red boxes), to account for the eastward propagation of the MJO. For the analysis of equatorial waves, five longitudes (Figure 1, coloured dashed lines) were selected to intersect different countries.

2.2.2 | MCS identification and tracking

Convective systems were tracked at hourly intervals using 10.4 μm T_b. Contiguous regions of cold cloud ($T_b < 233$ K) were tracked spatio-temporally using the tracking algorithm documented in Stein *et al.* (2015). Tracking the systems using T_b as opposed to precipitation allows storms to be better captured throughout their lifetime and provides the ability to track the large-scale organisation of systems, even when precipitation underneath the cold cloud shield is spatially or temporally intermittent (Klein *et al.*, 2018). After projecting forward existing clusters from time $t-1$ to time t using an optical flow technique, the tracking algorithm uses area overlap to determine which cloud clusters from time $t-1$ match with those at time t. When more than one cloud cluster at time t matches a cloud cluster at time $t-1$, the largest cloud cluster retains the storm ID and the other cloud cluster is defined as a child of the original (a split). When more than one cloud cluster at time $t-1$ matches one cloud cluster at time t, the cloud cluster at time t is given the storm ID of the larger cluster at time $t-1$ and the other cluster is defined as having merged. This process is not as sophisticated as the three-dimensional spatio-temporal multi-threshold detect and spread method of Fiolleau and Roca (2013) or the multi-threshold method of Feng *et al.* (2021) at identifying MCSs. However, we used size and rain rate thresholds to further classify storms as MCSs. The rainfall associated with each storm, $R(t)$, was determined by interpolating the IMERG rainfall onto the Himawari grid used for tracking and selecting just the pixels of the storm; that is, the rainfall is that found under the cold cloud pixels.

An MCS was classified as any storm where the contiguous region of cold cloud ($T_b < 233$ K) reaches an area of at least 10,000 km^2 at some point during its lifetime. The lifetime must be at least 6 hr and the associated rainfall must reach a mean rate over the cold cloud of at least 1 mm·hr^{-1} at some point during its life. The temperature and spatial thresholds chosen are comparable to prior studies within the Tropics (Crook *et al.*, 2019; Feng *et al.*, 2021; Fitzpatrick *et al.*, 2020; Roca *et al.*, 2014; Taylor *et al.*, 2017). Yuan and Houze (2010) identified MCSs at the mature phase without using tracking by identifying cold cloud with associated precipitation features that met certain thresholds. A comparison of thresholds on sizes and rain rates in various studies and our own is provided in Table 1.

Our tracking algorithm identifies systems that are in fact tropical cyclones (TCs). These were removed because the mechanisms of their genesis and maintenance are different to MCSs. The International Best Track Archive for Climate Stewardship (Knapp *et al.*, 2010) database was used to identify all TCs in the region during the period of our study. Tracked storms that overlap with a 5° (~500 km) radius of the cyclone centre at any time, and any of their descendant storms, were removed. This method removes all storms attributable to TCs, not just those within the TC structure, and these storms are referred to hereafter as TC-related storms. Some of these TC-related storms may propagate a considerable distance from the TC itself, even to the equatorial region where TCs would not be found. In total, we found 134,306 MCSs and 26,819 TC-related storms across southeast Asia during the whole 5 years, and 65,219 MCSs and 11,794 TC-related storms during our detailed analysis period of NDJFMA.

Statistics of the storms were gathered using the following definitions:

A, the area of cold cloud (i.e., $T_b < 233$ K) at each time;
R_a, the mean rain rate over the cold cloud area at each time;
T_{ba}, the mean brightness temperature over the cold cloud area at each time.

We present these storm variables averaged over the lifetime or over the time during which the storm is in a certain MJO phase. We used a Welch's t-test (Welch, 1947) to determine the significance of anomalies in different MJO phases at the 95% confidence level. For rainfall accumulations and numbers of storms the populations for this significance test are by day, whereas for storm properties the populations are from each storm.

TABLE 1 Comparison of thresholds used in tracking and identifying mesoscale convective systems (MCSs).

Study	T_b thresholds	Tracking	Rainfall	Further MCS criteria
Yuan and Houze (2010)	260 K, but look for minima within this of <220 K	None	AMSR-E PF >1 mm·hr^{-1}	HCC > 800 km^2 Overlapping PF > 2,000 km^2 and >70% of HCS area >10% PF area has rain >6 mm·hr^{-1}
Roca *et al.* (2014)	190–235 K	Three-dimensional detect and spread (30 min)	TAPEER-BRAIN under cloud pixels but per day	None
Taylor *et al.* (2017)	233 K	None	TRMM2A25 radar	Area >25,000 km^2
Crook *et al.* (2019)	OLR <167 W·m^{-2} (equivalent to 233 K)	Areal overlap (hourly)		Area >5,000 km^2
Fitzpatrick *et al.* (2020)	OLR <167 W·m^{-2} (equivalent to 233 K)	Areal overlap (hourly)	Modelled extreme rain rate at 1800 UTC >10 mm·hr^{-1}	Area >25,000 km^2
Feng *et al.* (2021)	225 and 241 K	Areal overlap (hourly)	IMERG PF >2 mm·hr^{-1}	CCS > 40,000 km^2 for more than four consecutive hours Contains PF > 100 km for more than four consecutive hours Heavy rain volume ratio and rain skewness > various thresholds
This study	**233 K**	**Areal overlap (hourly)**	**IMERG under cloud pixels**	**CCS > 10,000 km^2 Lifetime >6 hr Mean rain >1 mm·hr^{-1}**

Note: The present study is highlighted in bold.
Abbreviations: T_b: brightness temperature; AMSR-E: advanced microwave scanning radiometer for the Earth Observing System; PF: precipitation feature; CCS: cold cloud system; HCC: high cloud complex; HCS: high cloud system; OLR: outgoing long-wave radiation; IMERG: Integrated Multi-satellite Retrievals for the Global Precipitation Measurement.

2.2.3 | Equatorial wave identification

A dataset of equatorial waves was identified in ERA5 data by Yang *et al.* (2023), with wave types defined by a meridional mode number n: Kelvin waves ($n=-1$), WMRG waves ($n=0$), and Rossby-1 (Rossby) waves ($n=1$). Their theoretical structures are shown in Figure 2a,c,e. Following Yang *et al.* (2021), the 850 hPa u and v wind components for each wave type were reconstructed at six-hourly intervals. The amplitude and phase of each wave were calculated using appropriate variables (referred to as W_1 and W_2; see Table 2) at appropriate latitudes to characterise the wave state at our five selected longitudes (Figure 1). Similar datasets based upon different reanalysis sources have been used in previous studies (e.g., Ferrett *et al.*, 2020; Peatman *et al.*, 2021; Yang *et al.*, 2003, 2007a, 2007b, 2007c, 2021), and the accuracy of the method has been investigated comprehensively in Knippertz *et al.* (2022), where it performed well against other identification methods. Figure 2b,d,f shows the composite winds for each of the different wave types when they occur at 121.5°E and indicates that this method is capable of producing structures similar to the theoretical structures. However, we found that the divergence patterns are mostly opposite to the theoretical patterns in the case of WMRG and Rossby-1 waves because the du/dx term, which opposes the dv/dy term, is dominant for our waves whereas the dv/dy term is dominant for the theoretical waves. In the case of Rossby-1 waves our composites also have strong convergence/divergence patterns at the Equator, whereas for the theoretical structures the two terms exactly balance at the Equator. Differences are not surprising given that theoretical plots are for dry theory with no land and because the meridional e-folding width was chosen fairly arbitrarily in theoretical plots.

Amplitudes of W_1 and W_2 were normalised by their standard deviation over the entire study period, with active waves defined as having a standardised amplitude ≥1. Values of amplitude at selected longitudes were calculated as a mean of a 5° region centred on the chosen longitude. We examined the amplitudes of the waves at 850 hPa, following Ferrett *et al.* (2020) and Yang *et al.* (2021).

The phase of an active wave was calculated by taking the inverse tangent of W_1/W_2, such that the phase

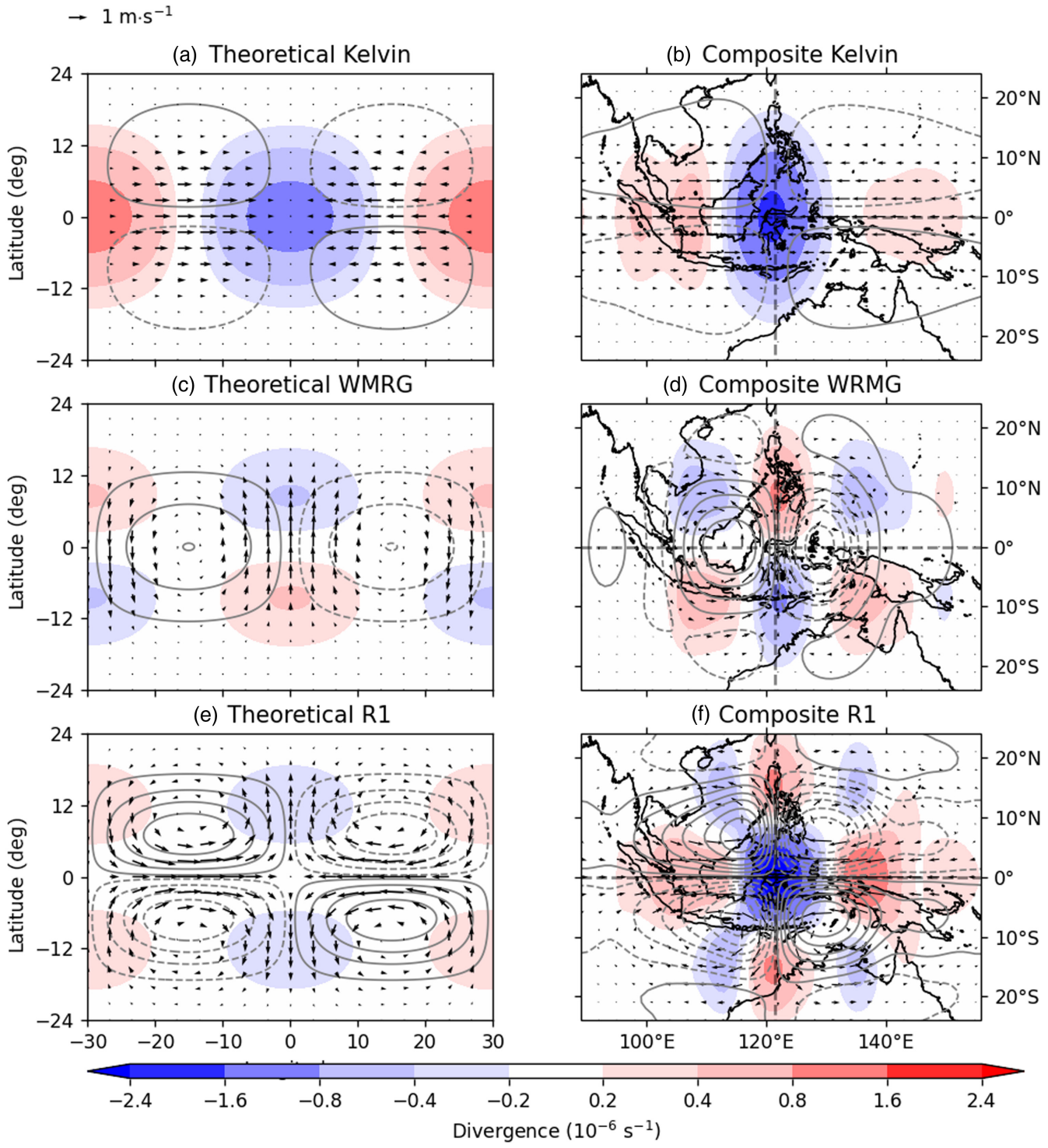

FIGURE 2 Wave structures of (a, b) Kelvin, (c, d) westward-propagating mixed Rossby–gravity (WMRG), and (e, f) Rossby-1 (R1) waves, with zonal trapping scale 6° and zonal wave number $k = 6$, for (a, c, e) theoretical structures and (b, d, f) composites from the Yang *et al.* (2023) dataset for all times with a wave present at 121.5°E. The filled contours indicate divergence (positive, red) and convergence (negative, blue), whereas the grey line contours indicate positive (solid) and negative (dashed) vorticity. The outermost line contours have absolute values of 0.2×10^{-5} s^{-1}, and the contours, moving towards the vorticity centres, have values of 0.8×10^{-5} s^{-1}, 1.4×10^{-5} s^{-1}, and 2×10^{-5} s^{-1} respectively. The black vectors indicate the wind field, with scale indicated by the key at the top left of the figure. The values in the figure are defined somewhat arbitrarily with q and v coefficients set to 1, as in Gill (1980). The figure is plotted following Yang *et al.* (2021, fig. 1)

TABLE 2 W_1 and W_2 for each equatorial wave mode, where u and v are zonal and meridional wind.

Wave type	W_1	W_1 latitude	W_2	W_2 latitude
Kelvin ($n=-1$)	u	0°N	$\frac{\partial u}{\partial x}$	0°N
Westward-propagating mixed Rossby–gravity ($n=0$)	$-u$	10°S	v	0°N
Rossby ($n=1$)	$-u$	0°N	v	8°N

can be defined by four quadrants in (W_1, W_2) space. For example, for Kelvin waves the four phases are where the wave structure is dominated by positive u, divergence, negative u, and convergence, respectively. For each active wave phase, the following rainfall fields were composited and the anomaly was calculated: all rainfall (from IMERG), MCS rainfall (from our MCS tracking database), TC-related rainfall (identified as described in Section 2.2), and other rainfall (the residual). Since the equatorial wave dataset is six-hourly, we estimated the total IMERG rainfall in the 6 hr period centred on the active wave's time step. Statistics such as A, T_{ba}, and R_a were not calculated for the MCSs in different equatorial wave phases since there are not enough storms present in different phases over the smaller areas involved at each longitude compared with the MJO analysis.

3 | RESULTS

3.1 | How much of the rainfall comes from MCSs?

Rainfall from the tracked MCSs represents 45–70% of total rainfall over the Maritime Continent islands (10°S–10°N) (Figure 3c,d) in line with previous findings across the Tropics (Nesbitt *et al.*, 2006; Roca *et al.*, 2014; Yuan & Houze, 2010). This is true in both NDJFMA and May–October (MJJASO). TC-related rainfall (Figure 3e,f) is only larger than MCS rainfall over the ocean north of 12°N and around the northwest coast of Australia and compares favourably with that found by Peatman *et al.* (2019) and Guo *et al.* (2017). Other rainfall (the remainder) (Figure 3g,h) contributes most north of 15°N in NDJFMA and south of 10°S in MJJASO, and contributes 40–75% between 10°S and 15°N.

We examined the importance of MCSs compared with rainfall associated with TCs in weather extremes by determining how much of the rainfall comes from MCSs and how much comes from TC-related storms when looking at days when the daily total rainfall accumulation exceeded different percentiles. To do this we found the percentage of total rain due to MCSs, TC-related storms, and other (the remainder) on each day over the land in nine different regions: Borneo, New Guinea, Sumatra, Malay Peninsula, Java, Myanmar and west Thailand (hereafter referred to as west Indo-China for brevity), east Thailand, Laos, Cambodia and Vietnam (hereafter referred to as east Indo-China for brevity), north Philippines, and south Philippines (Supporting Information Figure S1). The analysis was split into the two seasons, with the results the mean percentage of rainfall from MCSs, TC-related storms, and other on the days included in the different percentiles of total rainfall shown in Figure 4a (NDJFMA) and Figure 4b (MJJASO).

In NDJFMA, for all regions, the contribution to rainfall from MCSs increases for higher percentiles, with some regions approximately doubling their MCS contributions for the 99th percentile compared with all days, whereas the remainder contribution (other) decreases. For all regions except the Philippines, MCS rainfall is greater than TC-related rainfall at all percentiles. For all regions expect the Philippines and Indo-China, MCSs are the dominant contributor (>45%) to rainfall over all percentiles and contribute >55% for the 95th percentile, suggesting MCSs are the key phenomenon contributing to high-impact rainfall. In the Philippines (especially the north Philippines), TC-related rainfall becomes greater above the 90th percentile, contributing ~40% for the 95th percentile wet days.

In MJJASO, for all regions except Indo-China and the north Philippines, MCS rainfall is greater than TC-related rainfall at all percentiles, and its contribution increases for the higher percentiles; MCSs contribute >55% for the 95th percentile. However, the TC-related rainfall becomes more dominant above the 95th percentile in Indo-China and above the 70th percentile in the north Philippines, suggesting TC-related storms are the major contributor to high-impact rainfall in those locations.

Hereafter, we analyse NDJFMA only, when rainfall and the influence of the MJO on rainfall are high over the Maritime Continent.

3.2 | Locations and properties of different types of MCSs

Previous studies have shown the importance of MCS lifetime on contribution to rainfall (e.g., Coppin *et al.*, 2020; Feng *et al.*, 2021; Roca *et al.*, 2014). Roca *et al.* (2014)

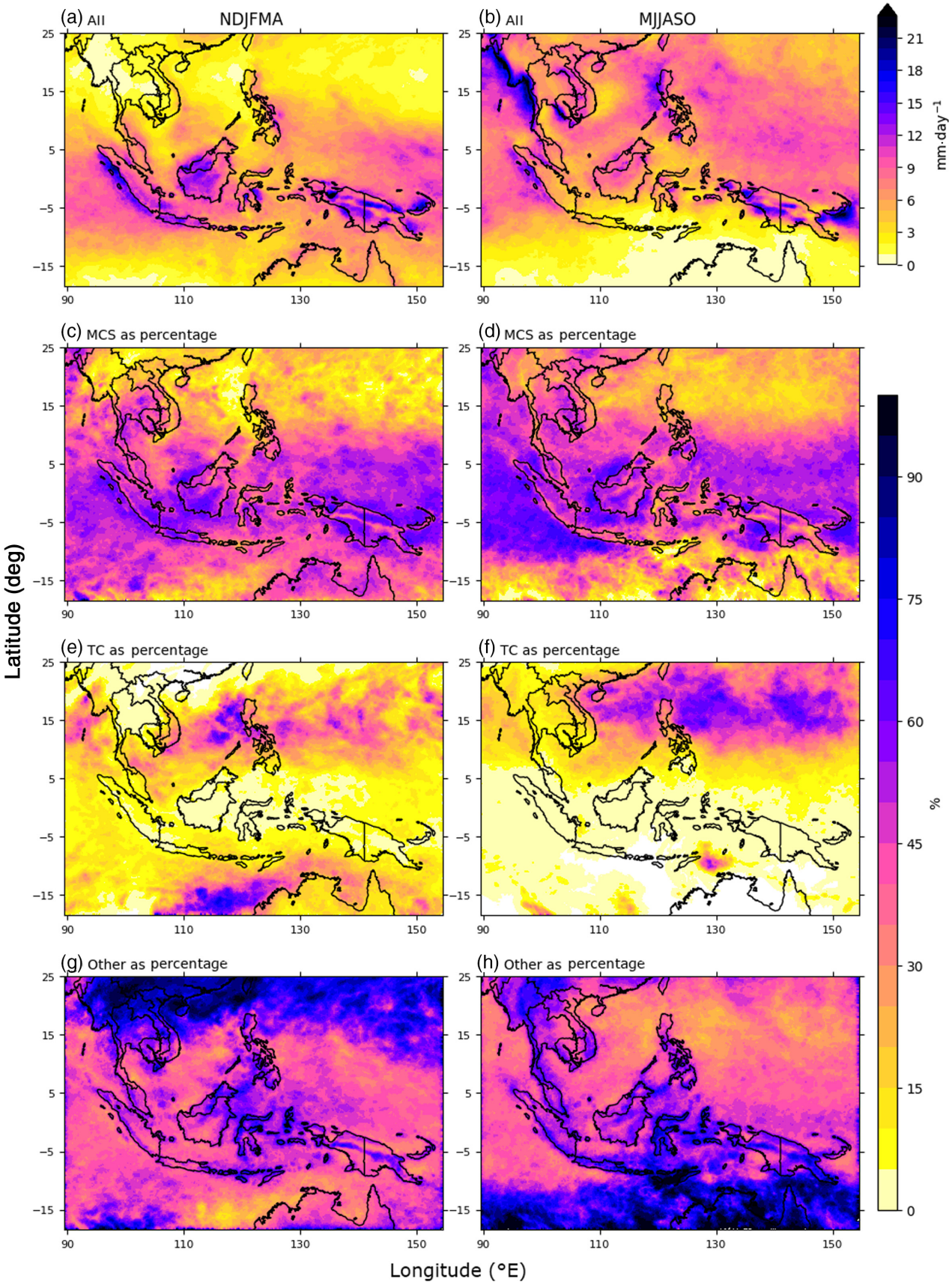

FIGURE 3 (a, b) Total rainfall (mm·day^{-1}), and rainfall as a percentage of the total for (c, d) mesoscale convective systems (MCSs), (e, f) tropical cyclone (TC)-related storms, and (g, h) other, for each season: (a, c, e, g) November–April (NDJFMA), and (b, d, f, h) May–October (MJJASO)

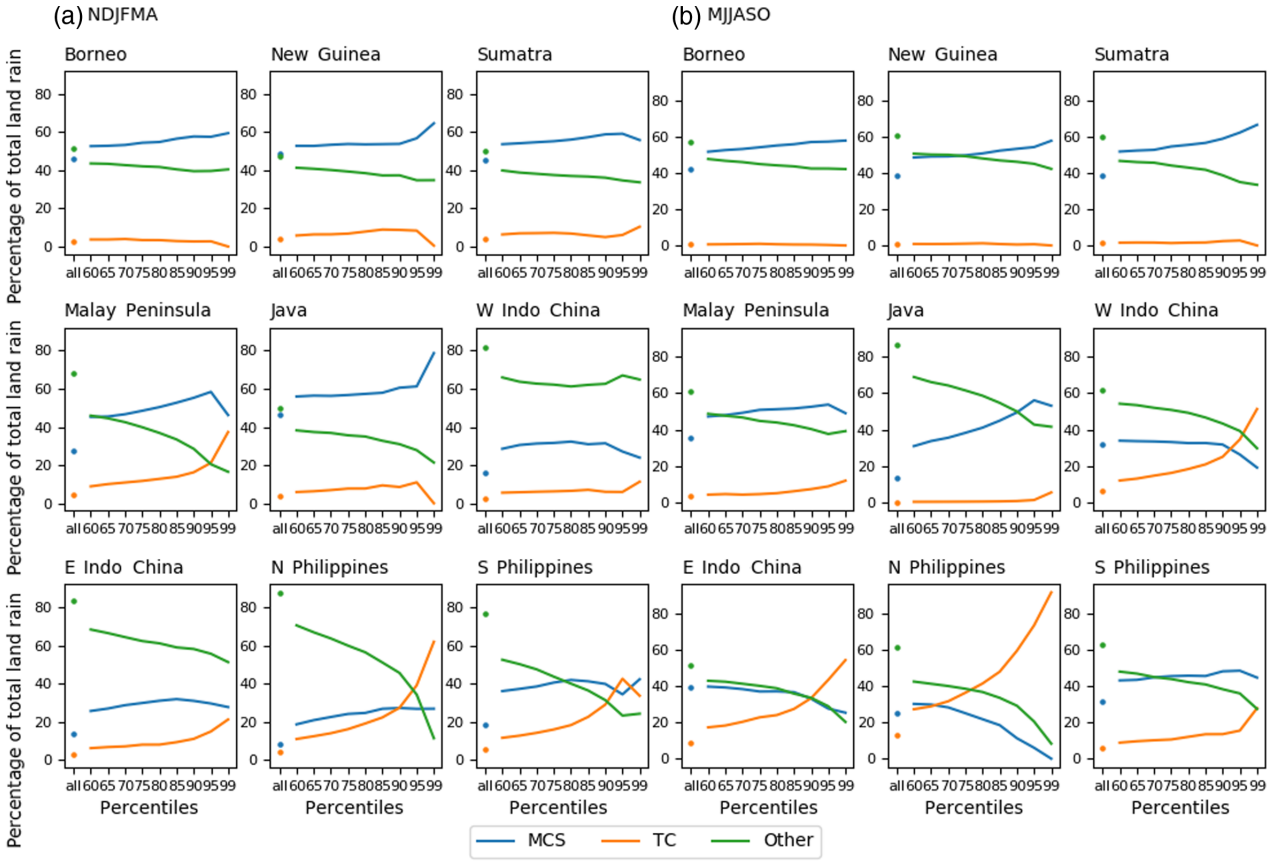

FIGURE 4 The percentage of total land rain as a function of total land rainfall percentiles in nine different regions that comes from mesoscale convective systems (MCSs) (blue line), tropical cyclone (TC)-related storms (orange line), and other (green line) in (a) November–April (NDJFMA) and (b) May–October (MJJASO). The dots on the left of each panel show the percentage of total rain for all days.

also suggested propagation distance has an impact on rainfall contribution, with MCSs propagating more than 250 km having the largest contribution. Also, fast-moving storms cause more problems for meteorological agencies, in that they can arrive at a location quickly without much warning; so, understanding these systems is important. Therefore, here, we examine the location and properties of different types of MCS based on lifetime and speed of propagation. Speed of propagation is determined by using the distance between the centroid of the storms at two well-separated times in the lifetime (ideally end and start) and dividing by the difference in time. When two clusters of cold cloud merge, the centroid of the new storm is unlikely to move much if one cluster is much larger than the other. However, if the two clusters are similar in size, the new centroid will be somewhere in the middle of the two clusters, and the new centroid will be some distance from the previous centroid even though the cold cloud field has not advected. Likewise, if a cold cloud cluster splits into two not dissimilar clusters, the centroid of the cluster maintaining the original ID will be some distance from the original centroid. Therefore, we determined the speed of propagation by taking sections of the lifetime where there were no mergers or splits of clusters of cold cloud that were more than one-third the previous size of the storm. The distribution of storms across different lifetimes and speeds (Figure 5) shows most of the storms have lifetimes of <24 hr and speeds <12 $m \cdot s^{-1}$. And those with shorter lifetimes have a greater spread of propagation speeds; that is, the fastest moving storms tend to be shorter lived (<24 hr).

MCSs were defined as one of four different types according to their speed and lifetime (fast-/slow-moving, short-/long-lived). The thresholds chosen for speed (7 $m \cdot s^{-1}$) and lifetime (12 hr) are based to some extent on previous studies (Crook *et al.*, 2019; Lafore *et al.*, 2017; Mathon & Laurent, 2001; Roca *et al.*, 2014; Yang *et al.*, 2017) and on the requirement to have a sufficient number of storms in each category to allow a statistically based analysis. Note, that an MCS that propagates at 7 $m \cdot s^{-1}$ for 12 hr would propagate about 300 km. MCSs tend to initiate in the early afternoon, so a lifetime of 12 hr distinguishes storms that survive overnight and into the next day. For MCSs that were either first or last seen at

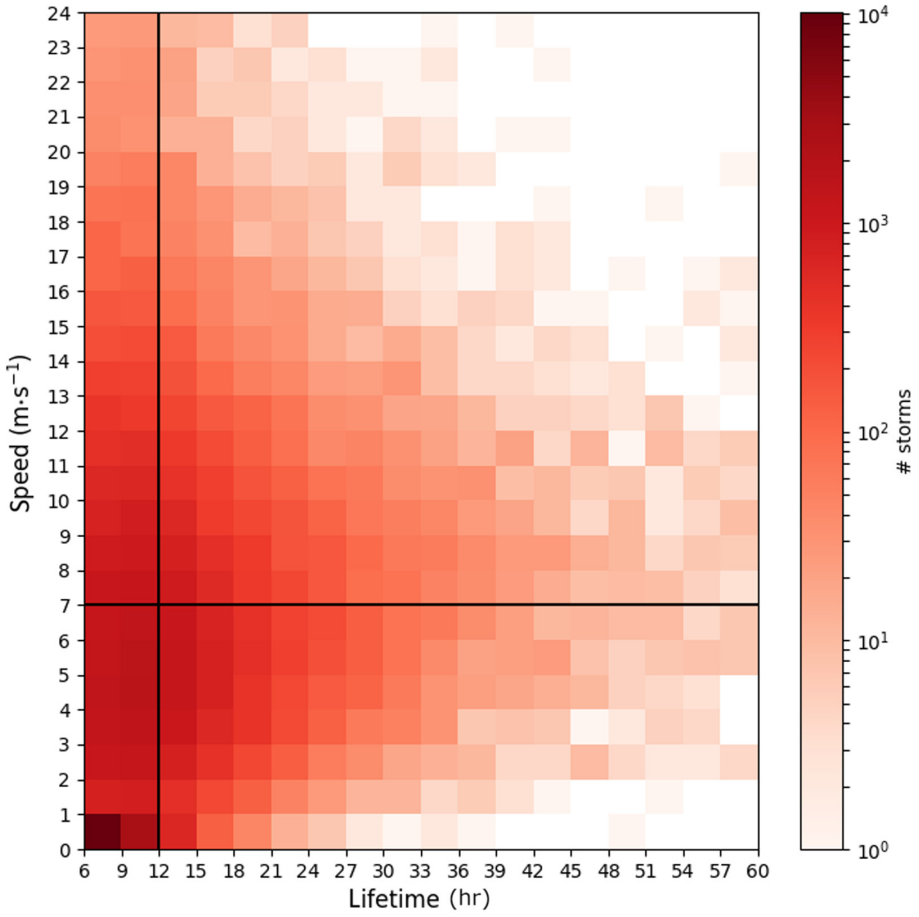

FIGURE 5 Two-dimensional histogram (percentage of mesoscale convective systems) of lifetimes and propagation speeds (in November–April). The thresholds of 12 hr for life and 7 m·s^{-1} for speed are shown as black lines.

the edge of the domain it is likely that we have not captured their full life. If the lifetime captured was greater than 12 hr they were classified as long-lived, otherwise they remained unclassified. As a result, 4% of the MCSs could not be classified. These unclassified storms only contributed just under 2% of the MCS rainfall. A lifetime threshold of 12 hr results in long-lived storms representing 34% by number and 85% by MCS rainfall contribution, and short-lived storms representing 62% by number and 14% by MCS rainfall contribution. This large rainfall contribution from long-lived MCSs is consistent with the results of Roca *et al.* (2014). A speed threshold of 7 m·s^{-1} was chosen to divide the population roughly in half in terms of storm numbers and contributions to rainfall, slow-moving storms representing 63% by number, 41% by rainfall contribution, and fast-moving storms representing 32% by number, 57% by rainfall contribution. During NDJFMA the combined (lifetime and speed) classification resulted in 11,415 (18%) fast-moving short-lived (Fast-Short) MCSs, 9,745 (15%) fast-moving long-lived (Fast-Long) MCSs, 28,672 (44%) slow-moving short-lived (Slow-Short) MCSs, and 12,652 (19%) slow-moving long-lived (Slow-Long) MCSs.

Distributions of the properties of MCSs as a function of lifetime and propagation speed are shown in Figure 6. The peak mean area A increases with lifetime but is less affected by speed. However, A drops off rapidly for slow-moving storms, whereas the distribution of A is much wider (longer tail) for the fastest moving storms. Very few short-lived or slow-moving storms have the largest areas. The peak mean T_{ba} decreases with increasing lifetime, but mean T_{ba} becomes less variable such that the coldest storms tend to be the shortest lived. Speed has little impact on peak T_{ba}, but the cold cloud tail is extended for slower moving storms such that the coldest storms tend to be slowest moving. The peak in mean R_a increases with lifetime, but mean R_a becomes less variable such that the highest values of mean R_a are only seen in storms with lifetimes <24 hr. The peak in mean R_a does not change with speed, but the high tail drops off more rapidly for the slowest moving storms, such that moderate to high values of mean R_a are more likely to be seen in faster moving storms.

Although Slow-Short MCSs are most numerous (44%) and Fast-Long MCSs least numerous (15%), by the very fact that long-lived MCSs are present for more time as well as tending to be larger on average (Figure 6a), the NDJFMA rainfall accumulations (Figure 7) of the long-lived MCSs (85% of MCS rain over the whole region) are much greater than those of the short-lived MCSs. Rainfall from all MCS

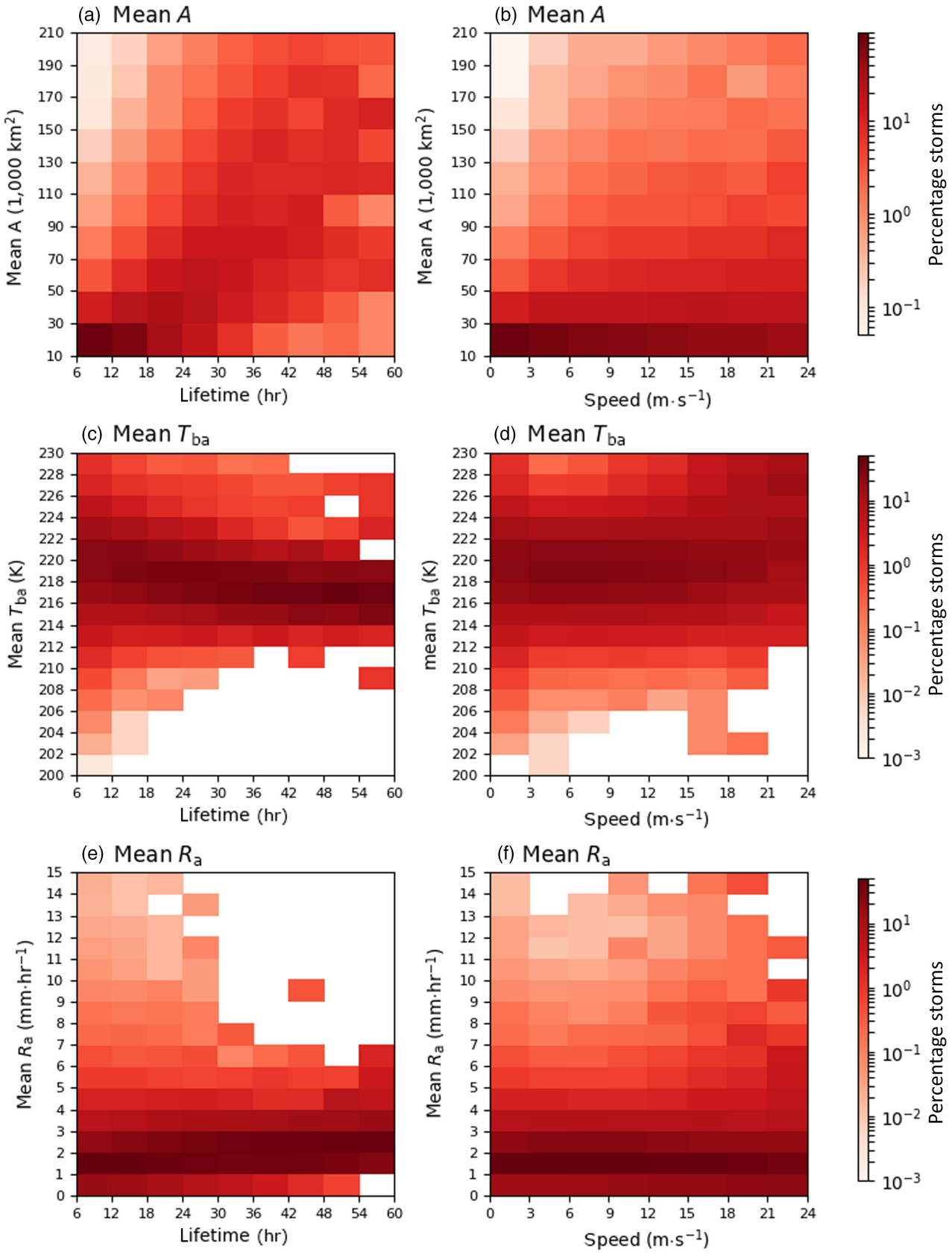

FIGURE 6 Histograms (percentage of mesoscale convective systems; in November–April) as a function of (a, c, e) lifetime and (b, d, f) propagation speed for (a, b) mean A, (c, d) mean T_{ba}, and (e, f) mean R_a. The distribution of each property is normalised in each column (lifetime bin or speed bin) because there are so few storms with long lifetimes or high speeds. Note the logarithmic scale to emphasise the extreme values.

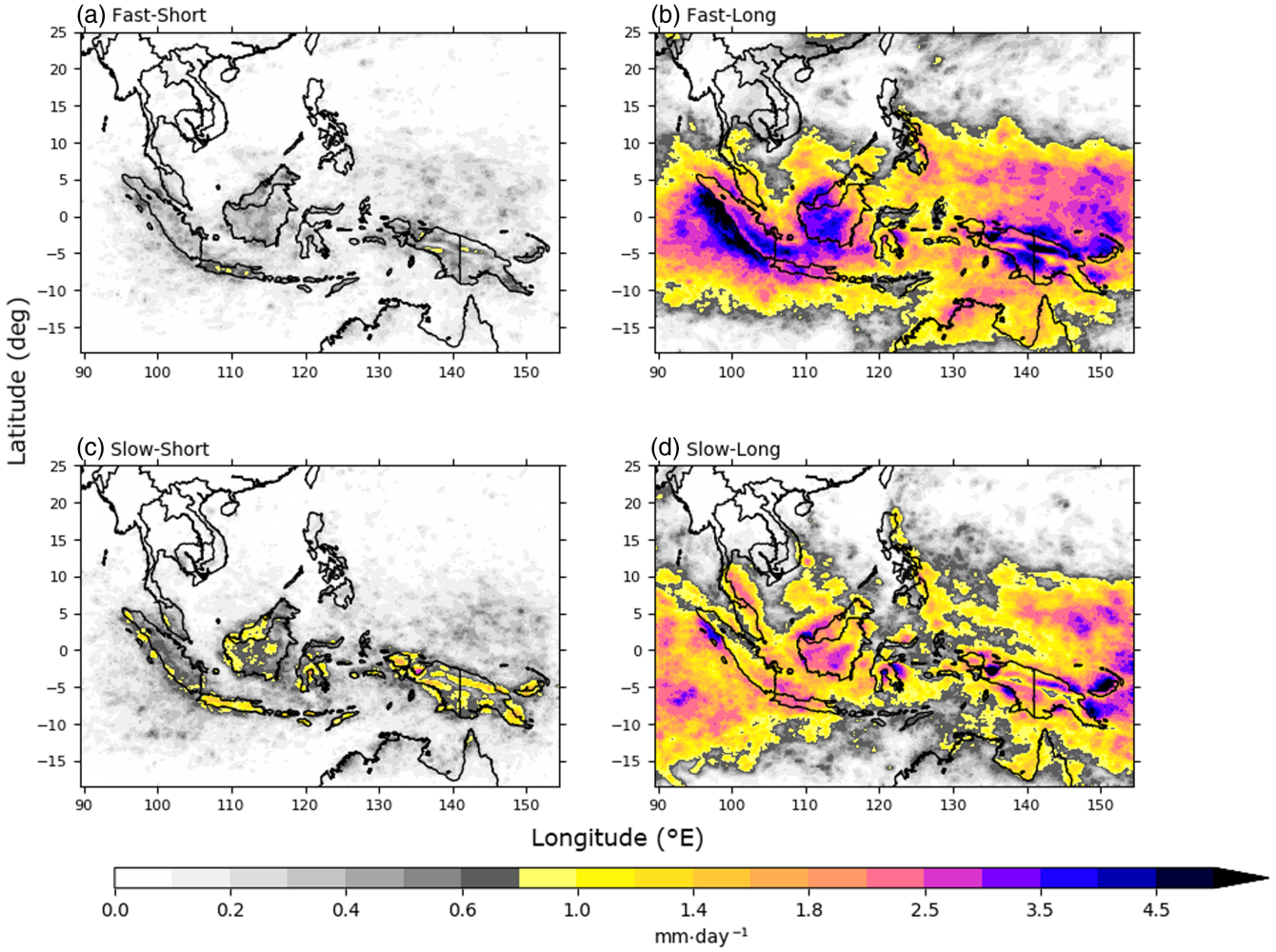

FIGURE 7 Rainfall accumulations per day from different types of mesoscale convective systems (in November–April): (a) Fast-Short, (b) Fast-Long, (c) Slow-Short, and (d) Slow-Long.

TABLE 3 Number of days and number of mesoscale convective systems (MCSs) in each region in each Madden–Julian oscillation (MJO) phase during November–April, 2015–2020.

MJO phase	1	2	3	4	5	6	7	8	No MJO
Number of days	39	73	83	105	92	69	94	70	282
MCSs per day									
West land	17.5	16.3	16.6	15.3	13.3	15.2	14.5	14.8	14.9
West sea	29.2	28.2	28.8	26.2	22.3	22.4	22.9	23.2	23.1
East land	16.6	16.3	15.3	12.7	13.1	12.3	12.4	14.2	14.0
East sea	36.3	35.6	37.7	36.5	30.8	29.6	28.8	28.9	31.7

types is greatest over or near the Maritime Continent islands. The Fast-Long MCSs produce most of the rain in the Maritime Continent and are particularly dominant over southern Sumatra and Borneo, and New Guinea. Cold cloud frequencies in terms of number of stormy hours per 30 days (not shown) have a similar, albeit more smoothed-out pattern.

3.3 | Impact of MJO phase

The number of days and number of storms per day in the West and East land and sea regions in each MJO phase are shown in Table 3.

Rainfall accumulation anomalies for each phase of the MJO are shown in Figure 8. Similar features are seen

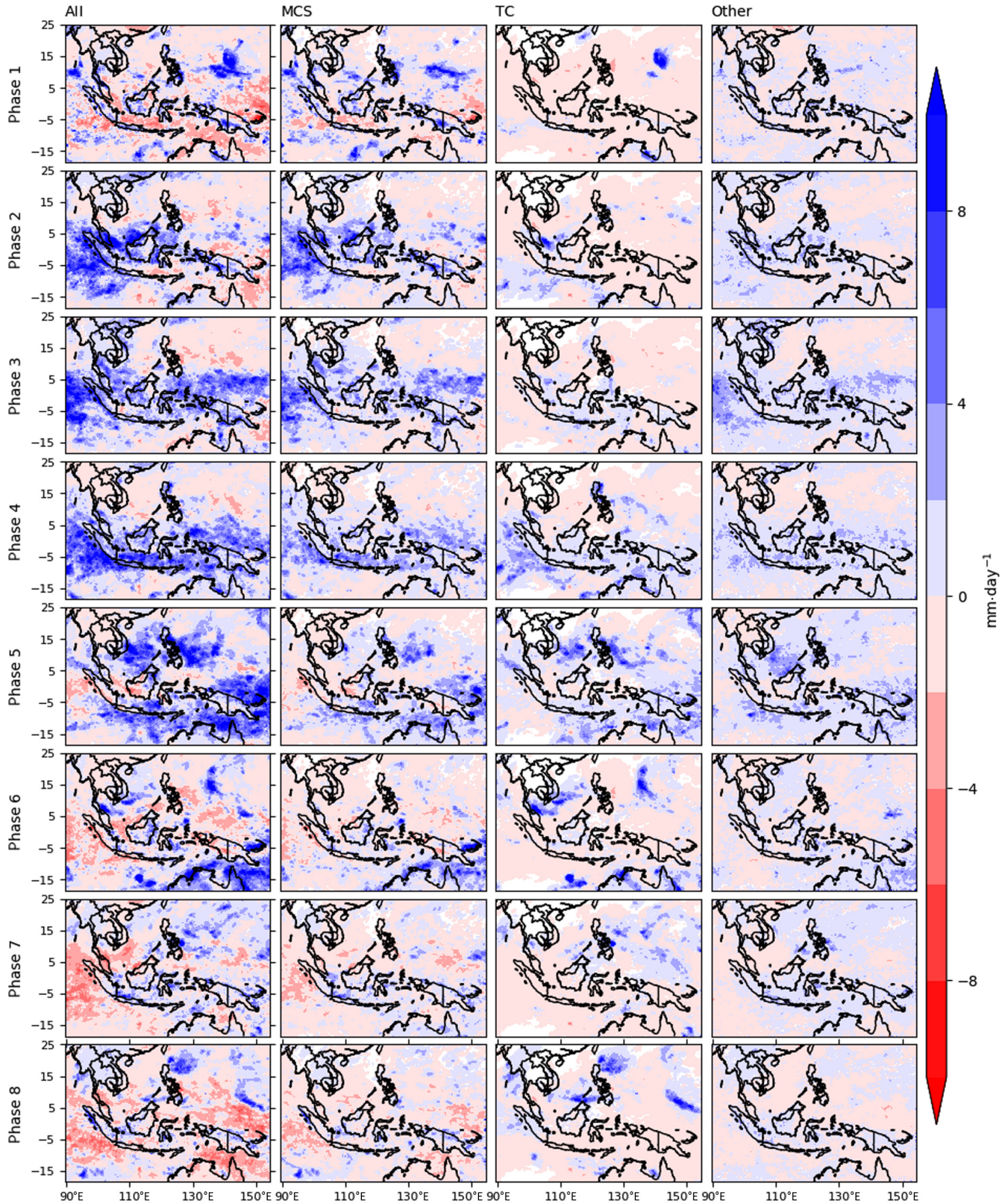

FIGURE 8 November–April rainfall anomaly by Madden–Julian oscillation (MJO) phase (rainfall for MJO phase minus rainfall for all MJO days) for all rainfall (left), mesoscale convective systems (MCSs; middle left), tropical cyclone (TC)-related storms (middle right) and the remainder (other; right).

in MCSs to that for all rainfall, although anomalies are greater for all rainfall as MCS rain accounts for only ~50% of the total rain. MCS rain moves west to east between phases 2 and 6 with less rain in phases 1, 7, and 8; land rain anomalies are ahead of ocean rain anomalies, with anomalies larger over ocean than land. TC-related rain has a less clear relationship with the MJO phase, although has dry anomalies in phases 1 and 2 and wet anomalies in phases 4 and 5. Other (the remainder) rain has a similar overall pattern to MCS rain, although of reduced amplitude because it partly comes from deep convection storms that are too short-lived and too small to qualify as an MCS.

These MCS rainfall features are summarised in Figure 9 for the two regions (West and East) over land and ocean. In the West region the MCS rainfall is significantly greater in phases 2–4 than in all MJO days, over both land and sea; and it is significantly lower in phases 5, 7, and 8 over land, and in phases 1 and 6–8 over sea. The largest anomaly is in phase 2, in agreement with total rainfall (Peatman *et al.*, 2014, fig. 11b). In the East region, significantly higher MCS rainfall occurs in phases 2–4 over land and in phases 3–5 over sea, and significantly lower MCS rainfall occurs in phases 6 and 7 over land and phases 7 and 8 over sea. The variations with MJO phase are smaller in the east than the west, consistent with the tendency of the eastward-propagating MJO signal to decay as it propagates over the Maritime Continent (DeMott *et al.*, 2018). MCS rainfall patterns are similar to total rainfall (cyan line).

Rain anomalies are dominated by long-lived storms, and the different types behave in broadly similar ways in the different phases (not shown). These rain anomalies for the long-lived MCSs are summarised along with their properties in different MJO phases for land and sea for the two subregions in Figures 10 (West) and 11 (East).

Rainfall accumulations over the West region (Figure 10a–d) are mostly higher in phases 2–4 and lower in phases 5–8 (and phase 1 for sea), but not always significantly, with the anomalies being greater and more significant for the Fast-Long MCSs than the Slow-Long MCSs. The total MCS rainfall is highest in phase 2 and is dominated by the Fast-Long MCSs. Over land, Slow-Long MCSs have their lowest rainfall accumulations in phase 5, whereas Fast-Long MCSs have lowest rainfall accumulations in phase 8. The rainfall anomalies are more statistically significant over sea than over land, likely due to the greater number of storms over sea.

There are more MCSs in phases 1–3 and less in phases 5–8, especially in phase 5 (Table 3). However, we find there is a significant difference in the propagation speed of MCSs in different phases, resulting in a greater proportion of fast-moving MCSs and lower proportion of slow-moving MCSs in phases 2–4 and a lower proportion of fast-moving MCSs and greater proportion of slow-moving MCSs in phases 7 and 8 for both land and sea (not shown). We did not find a significant shift in the proportion of long-lived MCSs in any phase. The number of stormy hours per day (Figure 10e–h), which is representative of the number of MCSs (although also dependent on lifetime but not on area) follows the pattern of rainfall anomalies well for Fast-Long MCSs (Pearson correlation coefficient $\rho = 0.9$ for land, $\rho = 1.0$ for sea) and moderately well for Slow-Long MCSs over land ($\rho = 0.5$), but does not explain the rainfall anomalies of Slow-Long MCSs over sea ($\rho = 0.2$). The anomalies are similar for both fast- and slow-moving MCSs and larger over the sea than land.

Mean R_a is higher in some of phases 2–4 and lower in phases 1, 5, and 6 and higher again in phase 8 for both fast- and slow-moving MCSs over both land and sea (Figure 10i–l) and is particularly high in phase 2 for the Fast-Long MCSs. This follows the pattern of rainfall accumulation in phases 1–5 but not in phases 6–8. In phase 8, when mean R_a is high, MCSs have lower mean A and lower storm numbers. Mean R_a is weakly correlated with rainfall anomalies for the Fast-Long MCSs over sea but poorly correlated in other cases.

Mean A is highest in phases 2–5 and low in phases 1, 7, and 8 and is moderately to strongly correlated ($0.6 \leq \rho \leq 0.7$) with rainfall accumulation (Figure 10m–p) for all but Slow-Long MCSs over land. For Slow-Long MCSs over sea, mean A best correlates with rainfall anomalies. The anomalies in A are greater for Fast-Long MCSs than for Slow-Long MCSs.

In summary, in the West region, for Fast-Long MCSs, the storm numbers, mean R_a, and mean A generally work together (positive ρ) to produce the rain accumulation anomalies, whereas for Slow-Long MCSs the different properties balance to give the rainfall anomalies. The Fast-Long MCSs are the dominant contributor to the rainfall anomalies due to a shift to faster moving storms in the convectively active phases and slower moving storms in the inactive phases.

Rainfall accumulations over the East region show less significant variability compared with the West region, but anomalies are still more significant over sea than land (Figure 11a–d). Over land, high anomalies are found in phases 2–4 for both Fast-Long MCSs and Slow-Long MCSs, and low anomalies are found in phases 6–8 for Fast-Long MCSs and phases 5–7 for Slow-Long MCSs. Over sea, high anomalies are found in phases 3–5 and low anomalies occur in phases 6–8 for Fast-Long MCSs and phases 1 and 2 and phases 7 and 8 for Slow-Long MCSs. Both Slow-Long and Fast-Long MCSs contribute to the rainfall anomalies, although the significant negative anomaly in phase 6 for total MCS rainfall over land is dominated by the negative

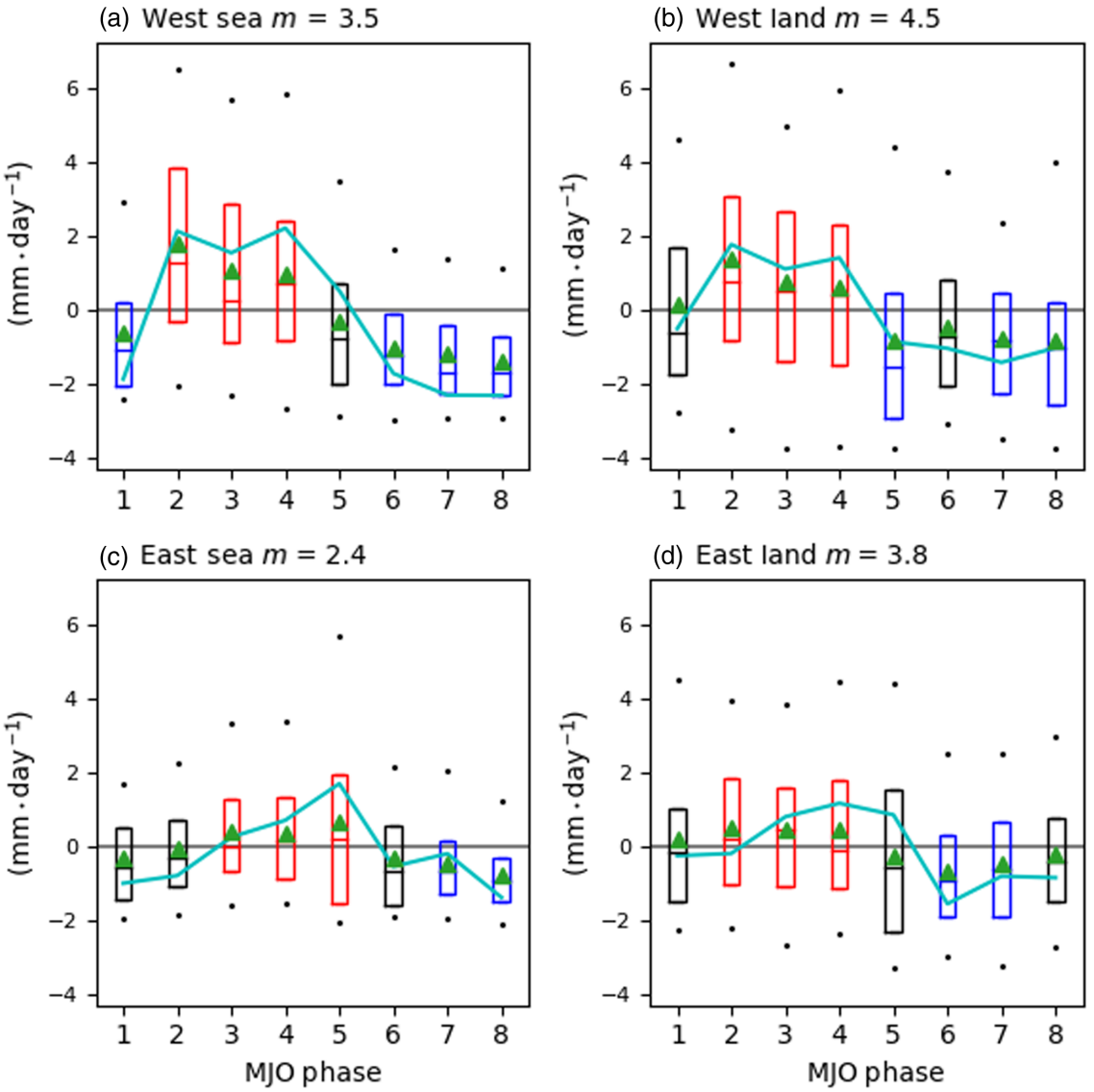

FIGURE 9 November–April mesoscale convective systems rainfall anomaly by Madden–Julian oscillation (MJO) phase (rainfall for MJO phase minus rainfall for all MJO days) averaged over (a, c) sea and (b, d) land and the two regions (a, b) West and (c, d) East. Boxes show median and interquartile range, dots show 5th and 95th percentiles, and green triangles show the mean. Red (blue) boxes indicate that the rainfall accumulation is statistically significantly higher (lower) in that phase compared with all active phases using a Welch's t-test at the 95% confidence level. The mean m over all the active phases is given in the title. The cyan line shows the mean anomaly of total rain in each phase.

anomaly for Slow-Long MCSs, and the significant positive anomaly in phase 5 for total MCS rainfall over sea is dominated by the positive anomaly for Fast-Long MCSs. The peaks and troughs occur slightly later over sea than over land.

The number of storms over East land is high in phases 1–3 and low in phases 4–7, and over East sea is high in phases 1–4 (particularly high in phase 3) and low in phases 5–8 (Table 3). However, we see a greater proportion of fast-moving MCSs in phases 5 and 6 and lower proportion in phase 8 over land and a greater proportion of fast-moving MCSs in phases 2 and 5 and lower proportion in phase 8 over sea (not shown). We also see a significant increase in the proportion of long-lived MCSs in phase 7 and a decrease in phase 3 over sea (not shown). These shifts between types impacts the number of stormy hours, which correlates ($\rho \geq 0.5$) with the rainfall anomalies for both Fast-Long and Slow-Long over both land and sea (Figure 11e–h).

Mean R_a shows a wave with highs in phases 8 and 1–3 over land and phases 2–4 over sea, and lows in phases 5–7 (Figure 11i–l). Mean R_a correlates moderately well for both types of MCS over land but only Fast-Long MCSs over sea. High mean R_a in phases 1 and 8 is compensated by low mean A, and low mean R_a in phases 5 and 6 is compensated by high mean A.

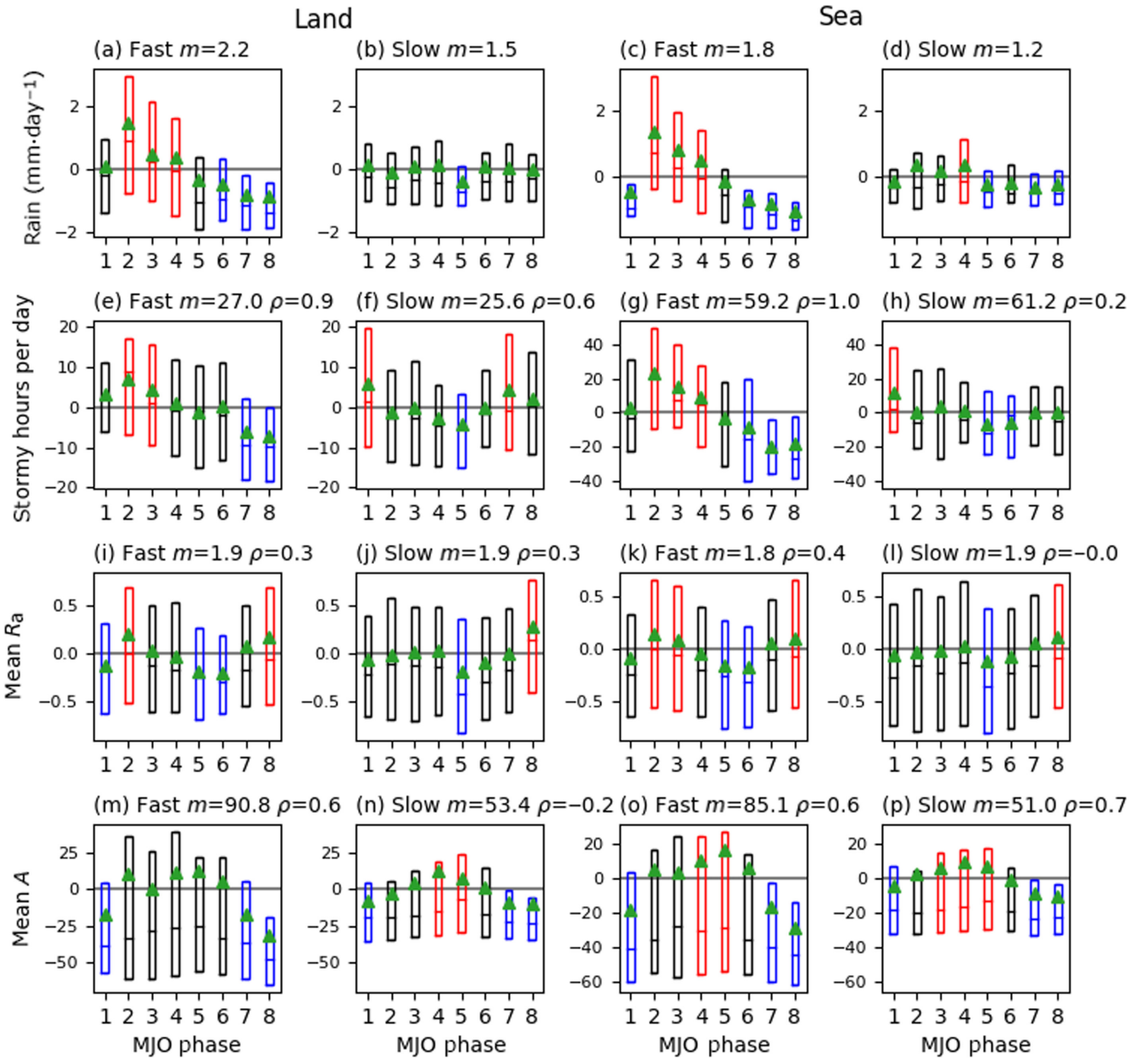

FIGURE 10 November–April mesoscale convective system (MCS) attributes by Madden–Julian oscillation (MJO) phase of long-lived MCSs over the West region (land in left two columns, sea in right two columns, split by MCS propagation speed – fast to the left and slow to the right). Anomalies of (a–d) rain accumulations and (e–h) number of stormy hours per day. Storm properties averaged over times when storm area is ≥10,000 km^2: (i–l) mean R_a, and (m–p) mean A. Boxes as in Figure 8, except 5th and 95th percentiles are not shown to aid clarity of interquartile range. Means m and Pearson correlation coefficients ρ between the mean variable and the mean rain anomaly (a–d) over the MJO phases are given in the titles.

Mean A follows a similar pattern as in the West region, but peaking slightly later in phases 5 and 6 and with lowest values in phases 1 and 8 (Figure 11m–p). In this region, mean A is strongly anticorrelated with rainfall accumulations for Slow-Long MCSs over land but moderately positively correlated for Slow-Long MCSs over sea and Fast-Long MCSs over both land and sea.

In summary in the East, for Fast-Long MCSs, the storm numbers, mean R_a, and mean A generally work together (positive ρ) to produce the rain accumulation anomalies, whereas for Slow-Long MCSs the different properties balance to give the rainfall anomalies. This is the same behaviour as seen in the West. However, compared with the West, over East land the Slow-Long MCSs have stronger positive correlation between rainfall accumulation and mean R_a, and stronger negative correlation between rainfall accumulation and mean A, and over the East sea, the Slow-Long MCS have stronger

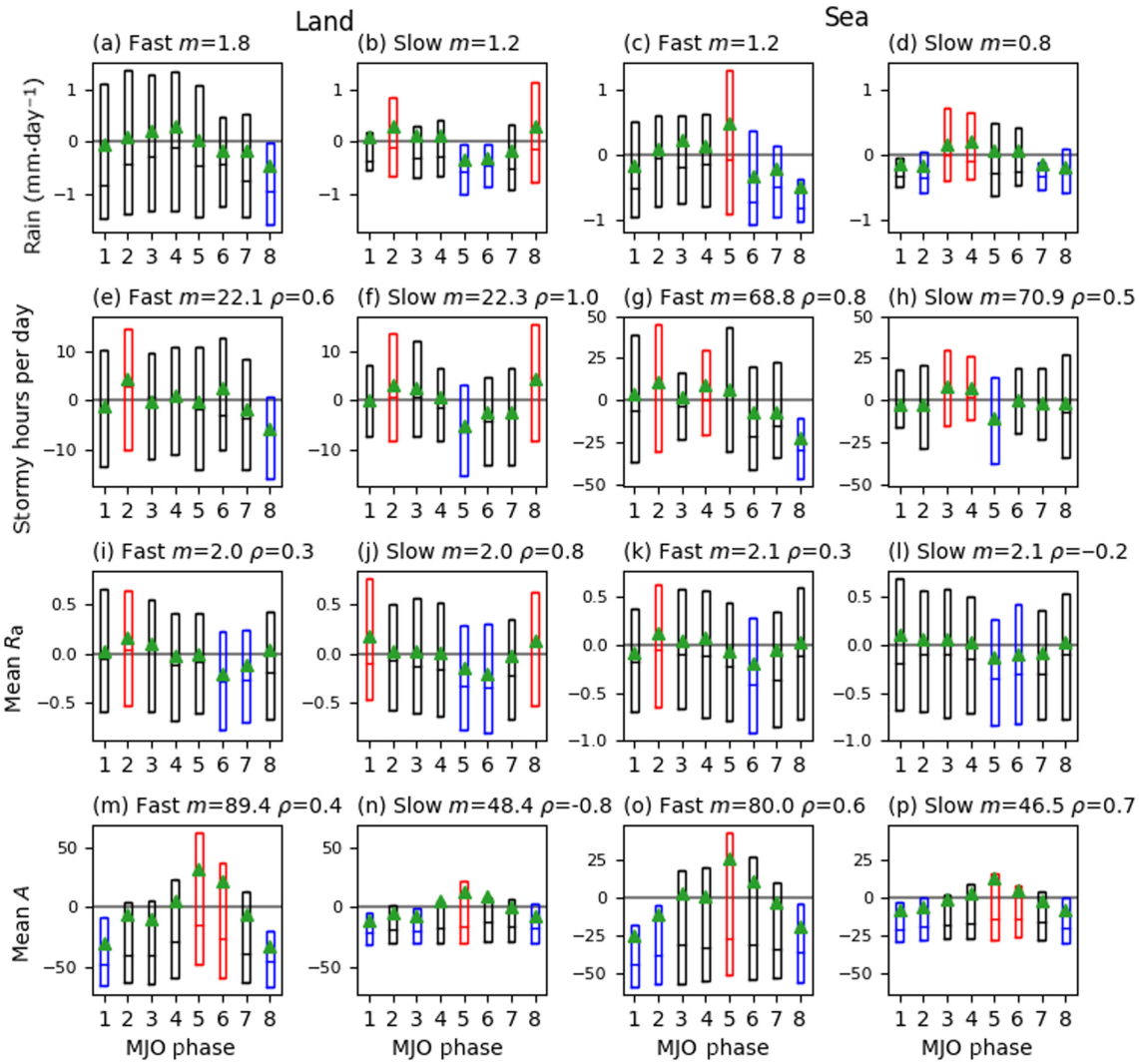

FIGURE 11 The same as in Figure 10 but over the East region.

correlation between rainfall accumulation and number of storms.

We found mean T_{ba} in both regions is lower (deeper convection) in phases with higher rainfall anomalies and higher (shallower convection) in phases with lower rainfall anomalies (not shown). In the West region, mean T_{ba} is strongly anticorrelated (i.e., intensity of convection is strongly positively correlated) with the rainfall, whereas in the East region this relationship is much weaker, especially over land.

3.4 | Impact of equatorial waves

Table 4 shows the number of waves at each six-hourly time interval that were identified as active (amplitude ≥1) at each of the subregions illustrated in Figure 1.

Kelvin waves are characterised by alternating regions of convergence and divergence (see Figure 2a). Low-level convergence will enhance precipitation by generating updraughts associated with moist convection, which will result in rainfall, whereas divergence at the same level will cause updraughts to weaken and dissipate and thus result in drier regions. Our analysis characterises the wave phase as dominated by either convergence or divergence, or positive or negative u, as highlighted in Table 2.

Consistent with the aforementioned argument, Figure 12 shows anomalies associated with the different phases of Kelvin waves at low levels (850 hPa): a strong wet anomaly in the Kelvin wave phase associated with convergence (Figure 12d,h,l,p,t) and a corresponding dry anomaly in the phase associated with divergence (Figure 12b,f,j,n,r). For positive u there are smaller wet anomalies to the east of the specified longitude that are associated with the anomalies from the convergence phase to the east. This pattern appears in the Kelvin wave rainfall anomalies at all longitudes, but it is at its most

TABLE 4 Number of 6-hr periods at each selected longitude (see Figure 1) where an active phase in a given phase exists.

Subregion	$-\frac{\pi}{4} < \varphi < \frac{\pi}{4}$	$\frac{\pi}{4} < \varphi < \frac{3\pi}{4}$	$\frac{3\pi}{4} < \varphi < \frac{5\pi}{4}$	$\frac{5\pi}{4} < \varphi < \frac{7\pi}{4}$
Kelvin wave phase	u **+ve at 0°N**	**Divergence**	u **−ve at 0°N**	**Convergence**
100.5°E	558	414	516	434
108.5°E	544	454	562	432
115.5°E	530	460	556	461
121.5°E	562	440	569	467
141.5°E	505	428	568	460
WMRG wave phase	ζ **−ve at 0°N**	v **+ve at 0°N**	ζ **+ve at 0°N**	v **−ve at 0°N**
100.5°E	438	449	419	485
108.5°E	415	446	431	325
115.5°E	442	448	400	474
121.5°E	437	464	431	461
141.5°E	422	417	423	441
Rossby-1 wave phase	u **−ve at 0° N**	v **+ve at 8°N (**v **divergence)**	u **+ve at 0°N**	v **−ve at 8°N (**v **convergence)**
100.5°E	528	503	531	483
108.5°E	509	406	526	427
115.5°E	481	410	520	429
121.5°E	548	414	517	431
141.5°E	548	439	490	396

intense for the westmost longitude over Sumatra (100.5°E; Figure 12a–d). This matches the observation in Section 3.3.1 that anomalies are generally stronger in the West region than in the East region and corresponds with the decrease in the Kelvin wave winds' standard deviations from west to east.

The rainfall anomalies are divided into different rainfall categories in Figure 13, which focuses on the westmost longitude centre at 100.5°E where the anomalies are strongest. The anomalies can be largely attributed to a combination of MCS and other rainfall, but there is also a smaller signature of enhanced wetness in the convergence phase in the TC-related rainfall, which may be due to MCSs associated with TC systems being classified as TC-related rainfall.

The total rainfall anomaly in all subregions has a large contribution from other rainfall, which is neither associated with MCS nor TC-related rainfall. This other rainfall may be less organised convection, which can be triggered or reinforced by low-level convergence while not maintaining a significant structure for a long period of time, and similarly may be more easily dispersed by weak diverging winds, such as those induced by Kelvin waves. This may explain why the signal is more distinct than for MCSs, which have more internal structure and independent longevity. Smaller organised systems that do not meet our size or longevity thresholds for MCS classification may also contribute to the other rainfall. However, the fact that up to half of the rainfall anomaly during a Kelvin wave cycle is attributable to changes in MCSs shows that MCSs are of considerable importance in understanding and predicting rainfall associated with Kelvin waves. Although we could not perform statistical analysis on MCS properties in the different Kelvin wave phases owing to the small number of storms present in each phase at each longitude, we did find that the mean MCS frequency, mean R_a, and mean A of all the MCSs whose cold cloud pixels enclosed the longitude in question were larger in the convergence phase than in the divergence phase for all longitudes.

WMRG and Rossby-1 waves are characterised by cyclonic and anticyclonic vortices centred on the Equator for WMRG waves and opposing direction vortices either side of the Equator for Rossby-1 waves. The composited regions of convergence and divergence were found to be quite different from the theoretical regions in Figure 2, likely due to the strong mostly northeasterly background flow in the Northern Hemisphere and westerly background flow in the Southern Hemisphere, and to different relative amplitudes of the $\partial u/\partial x$ and $\partial v/\partial y$

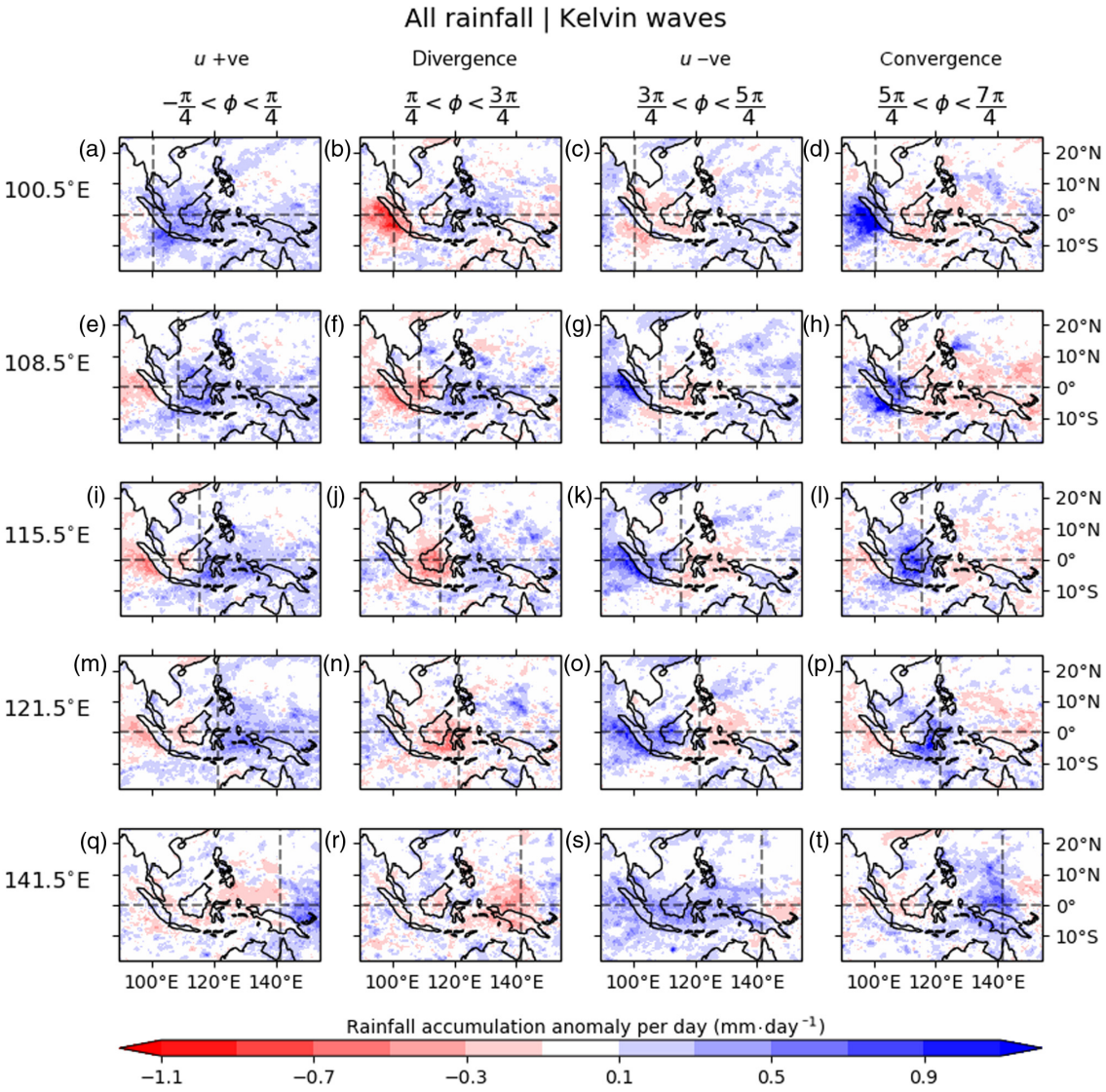

FIGURE 12 Integrated Multi-satellite Retrievals for the Global Precipitation Measurement rainfall anomaly composites across Kelvin waves of significant amplitude (standardised amplitude ≥1) at different phases of the wave (different columns) for the five longitude focus areas (different rows) (see Figure 1). Positive (blue) values indicate a wet rainfall anomaly and negative (red) values indicate a dry rainfall anomaly. The dashed lines indicate the latitude at which $W_1 = u$ and $W_2 = \partial u/\partial x$ are calculated, 0°N. The Kelvin wave propagates eastwards, moving through its phases from the left column to the right column as it propagates.

components compared with theory. We did not find the rainfall anomaly locations were related to the convergence locations but more related to the cyclonic vortex. We found that WMRG and Rossby-1 wave signals are dominated by TC-related rainfall, with greatest total rainfall anomalies in the positive vorticity phases (up to 70% of the total rainfall anomalies in the positive vorticity phase of WMRG waves, and up to 50% of the total rainfall anomalies in the Northern Hemisphere positive vorticity phase in Rossby-1 waves). On days where TCs are present (42% of the time when there was a WMRG or Rossby-1 wave present), the mean amplitudes of Rossby-1 and WMRG waves are around 10% larger than on days where there are no TCs, suggesting their strong connection with TCs as evidenced in Feng *et al.* (2023), who found that westward-moving equatorial waves were precursors in 60–70% of TC cases. On days with no TCs we found a similar pattern of total rainfall anomalies, albeit with lower amplitude. The effects of different phases of WMRG and Rossby-1 waves on rainfall (see Supporting Information Figures S2 and S3) are more complex than the effects of Kelvin waves, with interaction with topography, onshore/offshore propagation, and synoptic systems such as Borneo vortices likely to be playing a part. A clear pattern for TC-related rainfall anomalies is observed, whereas the pattern for MCS rainfall anomalies and other rainfall anomalies are less

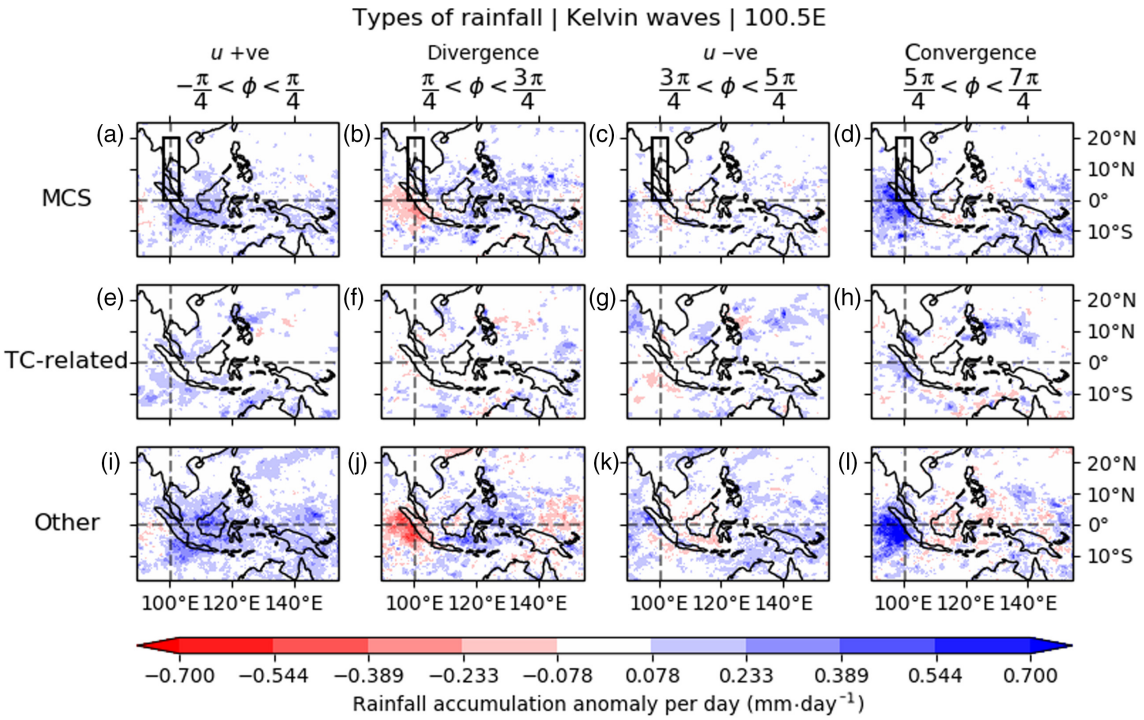

FIGURE 13 Rainfall anomaly composites across Kelvin waves of significant amplitude at 100.5°E, divided into three types of rainfall: (a–d) rainfall associated with mesoscale convective system (MCS) tracks, (e–h) rainfall related to tropical cyclones (TCs), and (i–l) rainfall associated with neither.

clear. Therefore, we further investigate rainfall anomalies for these wave modes on days when there are no TCs present.

Figure 14 shows a more quantitative measure of the impact of equatorial waves on MCS rainfall anomalies averaged within a 5°-wide box centred on the selected longitude between 0 and 20°N (the box illustrated in the top row of Figure 13) in each wave phase for Kelvin (Figure 14a), WMRG (Figure 14b), and Rossby-1 (Figure 14c) waves. Although 10°S–10°N could be used for Kelvin waves, we chose to use the same box for all wave modes to make comparison easier. The lines represent the anomaly using all days for Kelvin waves but non-TC days for WMRG and Rossby-1 waves. In the convergence phase of the Kelvin wave (rightmost points), all regions show a robust positive precipitation anomaly (20–30% of total rainfall anomaly) and a robust negative anomaly (20–70% of total rainfall anomaly) in the divergence phase. Different regions have a wider spread of MCS rainfall anomalies in the phases dominated by easterly and westerly zonal winds, however. For example, over Sumatra and Borneo, westerly winds appear to increase rainfall anomaly directly over the selected longitude (possibly due to interaction with the land or by enhancing wind-dependent surface energy fluxes over regions where the basic zonal wind is westerly, for example; Yang *et al.*, 2007a), whereas over Papua New Guinea, although there is a wet anomaly to the east, there is a slight dry anomaly over the selected longitude.

Different regions do not show the same behaviour of total rainfall or MCS rainfall in all phases of WMRG or Rossby-1 waves, suggesting that behaviour is sensitive to the geography of the region. For WMRG phases, the sign of the MCS rainfall anomaly matches the sign of the total rainfall anomaly with positive anomalies in the positive vorticity phase and negative anomalies in the negative vorticity phase for all longitudes except 115.5°E and 121.5°E, which show the opposite behaviour. WMRG MCS rainfall anomalies are 0–50% of total rainfall anomalies on non-TC days. For Rossby-1 phases, most regions show an appreciable increase in MCS rainfall anomaly in the Northern Hemisphere positive vorticity phase and a decrease in the meridional divergence phase (10–50% of total rainfall on non-TC days), but the amount of rainfall contributed by MCS anomalies is not as large as that in the Kelvin wave convergence phase. The range of the total rainfall anomaly across WMRG and Rossby-1 phases on TC days is 3–4 mm·day^{-1}, whereas on days where there are no TCs, the range of the total rainfall anomaly decreases to around 1 mm·day^{-1}. MCS rainfall anomaly also decreases on days with no TCs compared with those with TCs (not shown).

We suggest that Kelvin waves more strongly modulate MCS rainfall than WMRG or Rossby-1 waves do because the Kelvin wave structures typically have stronger

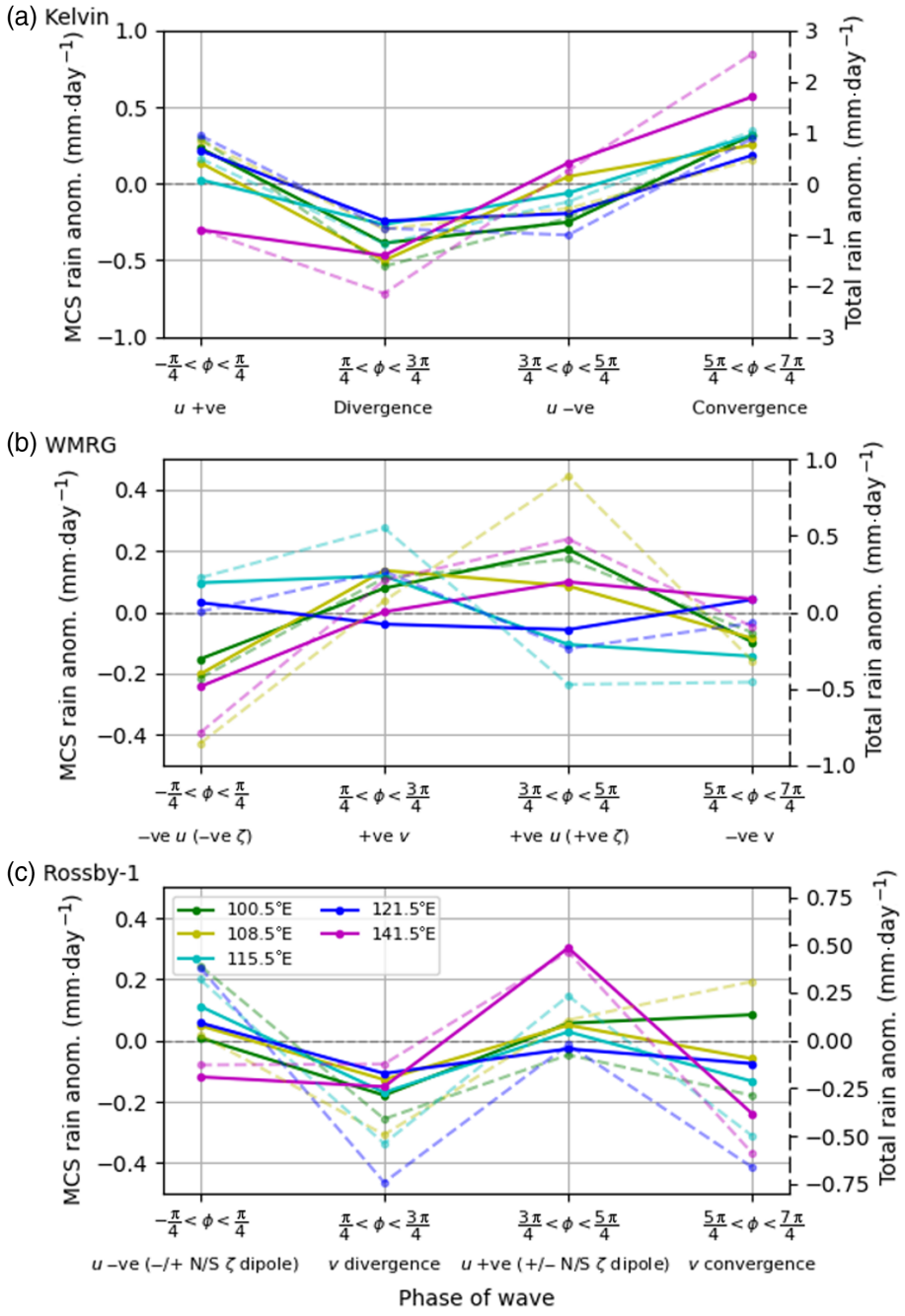

FIGURE 14 Rainfall anomalies in each phase (dashed lines: total rainfall; solid lines: mesoscale convective systems [MCS] rainfall) within a box of 5° width centred on the selected longitudes (represented by the different colours; see Figure 1) with latitude spanning from 0°N to 20°N (example shown in Figure 13) for (a) Kelvin, (b) westward-propagating mixed Rossby–gravity (WMRG), and (c) Rossby-1 waves. For WMRG and Rossby-1 waves, MCS anomalies are calculated on days when TCs do not occur.

convergence structures than the other types of waves (which can be seen in Figure 2). Low-level convergence (e.g., at 850 hPa, where we identify and locate these waves) is strongly associated with MCS initiation and development since it is essential to maintain the strong updraughts characteristic of MCSs. More convergence means stronger updraughts and greater organisation of the systems. Furthermore, Kelvin wave structures tend to be more vertically tilted than structures of WMRG and Rossby-1 waves are, which has been noted by previous studies examining their vertical structures (e.g., Kiladis *et al.*, 2009, Nakamura and Takayabu, 2022), and which can be seen in composites of the projected wave structures of the dataset we used (not shown). The greater tilt in the Kelvin wave structure allows for two things: First, the alignment of low-level convergence and upper level divergence facilitates the existence of deep, strong updraughts that are essential to deep convection. Second, the tilt results in significant vertical shear, which is effective in organising MCSs (e.g., Rotunno *et al.*, 1988). One final aspect of Kelvin waves that might explain their stronger alignment with MCS rainfall is simply the fact that Kelvin waves, unlike WMRG and Rossby-1 waves, occur in a latitudinal range with maximum amplitude on the Equator, where the greatest number of MCSs occur (see Figure 3).

In summary, the convergence phase of Kelvin waves appears to favour MCS rainfall by enhancing MCS frequency and storm-mean rain rates and areas, and their divergence phase suppresses MCS rainfall by reducing MCS frequency and storm-mean rain rates and areas. Rossby-1 and WMRG waves do not modulate MCS rainfall as strongly as Kelvin waves do, and patterns that do exist are sensitive to local geography of the area.

4 | CONCLUSIONS

In this article we present the importance of MCSs for rainfall in Southeast Asia (90–154°E, 18°S–30°N), demonstrate their contribution to high-impact rainfall, and show how they are affected by the MJO and equatorial waves. Understanding the influence of large-scale weather patterns on these storms is crucial for both aiding forecasting and improving climate models in a region that is prone to frequent high-impact weather. MCSs were tracked in the region by applying a tracking algorithm to Himawari-8 brightness temperature (10.4 μm) over a 5-year period between 2015 and 2020. MCSs are further defined as those tracked storms that last ≥6 hr, reach an area of 10,000 km^2 and a storm mean rain rate of 1 $mm \cdot hr^{-1}$. Storms associated with TCs were also removed. In total, 134,306 MCSs were tracked, including 65,219 MCSs in the boreal winter season of NDJFMA. The rainfall within each MCS was found using IMERG. We investigated the climatologies of MCSs with different lifetimes and propagation speeds. We classified the MCSs in this database according to their lifetime (with a 12 hr lifetime as the threshold between short-lived and long-lived storms) and propagation speed (with a 7 $m \cdot s^{-1}$ threshold between slow and fast storms). We then examined the impact of MJO phase and equatorial waves on the tracked MCSs.

MCSs account for 45–70% of total rainfall over the domain from 10°S to 10°N. This contribution was analysed as a function of the rainfall rate over land for nine locations across the domain. In general, the MCS contribution is higher on the wettest days (mostly >55% for the 95th percentile of total rainfall), showing the importance of MCSs for extreme weather. Long-lived MCSs dominate the rainfall contribution, accounting for around 85% of MCS rainfall, although only accounting for 34% by number. in line with Roca *et al.* (2014). Storms that are fast and long-lived contribute the most rainfall, especially over islands in the region. Long-lived MCSs also tend to have the lowest average brightness temperature, implying that they involve deeper convection, and the largest areas, whereas fast-propagating storms have the highest mean rain rates.

Analysis of the relationship between the MJO and MCSs shows that the MCS rainfall varies with MJO phase, but the variation is amplified considerably more in the West region than in the East region. The variation in rainfall associated with MCSs can be attributed to the number of storms, the area-mean rainfall rate within the storms, and the area of the storms. The contribution of each of these varies depending on the region and the class of MCS. In both the West and the East regions, for Fast-Long MCSs, these three properties generally work together (positive ρ) to produce the rain accumulation anomalies, whereas for Slow-Long MCSs the properties balance in more complex ways to give the rainfall anomalies. In the West region, a shift from slow-moving to fast-moving MCSs occurs during the active phases and vice versa during the inactive phases. This makes the Fast-Long MCSs the dominant contributor to the rainfall anomalies in the West region. We found MCSs generally propagate westwards in this region. The mean ERA5 wind at both 850 and 500 hPa is more easterly in phase 2 and less easterly in phase 7 (for 850 hPa, see Figure 8; Wheeler & Hendon, 2004), which likely causes the MCSs to propagate faster in phase 2 than in phase 7. We also found in both the West and East regions that the size of the MCSs peaks in phase 5, generally coinciding with the lowest rain rate and lowest total number of MCSs and lagging the peak in rainfall, suggesting that MCSs are strongly aggregated and have the largest anvils and stratiform rainfall contributions in phase 5. This is in agreement with the results of Virtz and Houze (2015), who found a shift to more stratiform contributions that lagged the peak in rainfall as an active MJO passed through the region. On examining the vertical wind shear (200 hPa minus 850 hPa) in the different MJO phases we found that the wind shear is greatest in phases 4–7, which would enhance the size of the anvil. Cheng *et al.* (2023) found an increase in frequency, size, and rain rate during the convectively active MJO compared with climatology but did not split the MJO into the eight different phases shown here. Our results show how these changes in different properties do not all occur in exactly the same MJO phases.

A strong correlation between high rain rates and low brightness temperature (deep convection) is observed in the West region, but in the East region the correlation is somewhat weaker.

Analysing the impact of equatorial waves on MCSs showed that equatorial Kelvin waves modulate MCS frequency and rainfall contribution considerably. The MCS rainfall anomalies increase when an active Kelvin wave is in its low-level convergence phase, and the largest rainfall anomalies are observed in the west of the region, as is the case for MJO modulation of MCS rainfall. MCS rainfall anomalies account for around 20–50% of the rainfall anomalies in $5 \times 20°$ regions centred on the locations where the waves were identified; Kelvin waves similarly modulate rainfall that is not associated with

MCSs or TCs. Convergence at 850 hPa is the defining feature of the convectively active phase of Kelvin waves. Such convergence is associated with all convective updraughts to maintain continuity, so it could be linked to all types of convective rainfall, including structures that are not classified as organised MCSs. Low-level convergence also serves to strengthen and intensify MCSs.

WMRG and Rossby-1 waves, however, do not modulate MCS rainfall anomalies as strongly, with MCS rainfall anomalies contributing to less than 20% of the total rainfall anomalies around the longitude of the active part of the wave when all days are considered. The rainfall anomalies in different phases of WMRG and Rossby waves are dominated by rainfall associated with TCs. We found that TCs were present 42% of the time when an equatorial WMRG or Rossby-1 wave was present, and these waves are often precursors to TC cyclogenesis (Feng *et al.*, 2023). On days with no TCs present, the MCS rainfall anomalies contribute up to 50% of the total rainfall anomaly but there are considerable differences in the behaviour across phases between different longitudes.

The enhanced MCS rainfall associated with the active phase of Kelvin waves corresponds with results seen in the literature (e.g., Cheng *et al.*, 2023; Nakamura & Takayabu, 2022), but studies, including Nakamura and Takayabu (2022), suggest that enhanced MCS precipitation is also increased in the active phases of Rossby-1 waves. It should be noted, however, that their study focuses on convectively coupled waves specifically, identifying the active phases through filtering of an infrared radiation dataset, whereas our wave identification focuses on projected wind structures at 850 hPa, which are not always associated with the low brightness temperatures of low cloud. It makes sense that, in examining only convectively coupled Rossby waves, their results show a stronger correlation of wave structures with mesoscale convection. The results of Cheng *et al.* (2023) suggest the Kelvin waves modulate MCS rainfall more strongly than the MJO, whereas we find the MJO modulates MCS rainfall slightly more strongly. However, they look at Kelvin waves during boreal summer, when these waves are stronger and also look at convectively coupled waves, unlike our study.

In summary, MCS rainfall over southeast Asia is a major contributor to extreme precipitation (>55% for the 95th percentile of total rainfall) especially south of 10°N, and is strongly modulated by the MJO (MCS anomaly ≥50%) and equatorial Kelvin waves (MCS anomaly: 20–50%). MCSs are subject to significant changes to their size, rain rate, and frequency due to the impact of the MJO. Given the difficulties of forecasting rainfall accurately in this region and the devastating impacts of heavy rain, these relationships provide forecasters with useful extra information that can be combined with the knowledge of existing or forecasted synoptic weather regimes. The skill of such combined forecasts of extreme rainfall would then be dependent on the skill of the forecast model to depict the equatorial waves and MJO, as well as the ability of the model to represent the relationships between MCSs and these large-scale weather features. These relationships may also be tested in the latest weather prediction models to aid model development.

ACKNOWLEDGEMENTS

Himawari data were provided by the Japan Meteorological Agency; we thank the ICARE Data and Services Center for providing access to the Himawari data used in this study. The equatorial wave dataset was produced as part of the Newton Fund project under the auspices of the WCSSP Southeast Asia project by Dr Gui-Ying Yang of the National Centre for Atmospheric Science, University of Reading. The ERA5 data were obtained from the Copernicus Climate Change Service, Climate Data Store (2023): ERA5 hourly data on pressure levels from 1940 to present. Copernicus Climate Change Service (C3S) Climate Data Store (CDS), DOI: 10.24381/cds.bd0915c6 (accessed on 03-April-2023). We also acknowledge K. R. Knapp, H. J. Diamond, J. P. Kossin, M. C. Kruk, and C. J. Schreck, 2018: International Best Track Archive for Climate Stewardship (IBTrACS) Project, Version 4. NOAA National Centers for Environmental Information. doi:10.25921/82ty-9e16 (accessed 03-April-2023) for the use of the TC database.

FUNDING INFORMATION

This work was carried out as part of the Severe Precipitation in South-East Asia (SPISEA) project, funded by the Met Office Weather and Climate Science for Service Partnership (WCSSP) Southeast Asia, as part of the Newton Fund. Peatman and Birch were also funded by the Terra-Maris project, funded by National Environment Research Council (NERC) grant NE/R016739/1.

CONFLICT OF INTEREST STATEMENT

The authors have no conflicts of interest to declare.

DATA AVAILABILITY STATEMENT

The MCS database that support the findings of this study are available from the corresponding author upon reasonable request. The code used to perform the MCS tracking is publicly available at https://github.com/thmstein/simple-track.

ORCID

Julia Crook https://orcid.org/0000-0003-1724-1479
Simon C. Peatman https://orcid.org/0000-0002-2511-7649

Thorwald H. Stein https://orcid.org/0000-0002-9215-5397
Gui-Ying Yang https://orcid.org/0000-0001-7450-3477

REFERENCES

Adhikari, P., Hong, Y., Douglas, K.R., Kirschbaum, D.B., Gourley, J., Adler, R. et al. (2010) A digitized global flood inventory (1998–2008): compilation and preliminary results. *Natural Hazards*, 55, 405–422. Available from: https://doi.org/10.1007/s11069-010-9537-2

Baranowski, D.B., Flatau, M.K., Flatau, P.J. & Matthews, A.J. (2016) Impact of atmospheric convectively coupled equatorial kelvin waves on upper ocean variability. *Journal of Geophysical Research – Atmospheres*, 121, 2045–2059. Available from: https://doi.org/10.1002/2015JD024150

Barlow, M., Wheeler, M.C., Lyon, B. & Cullen, H. (2005) Modulation of daily precipitation over Southwest Asia by the Madden-Julian oscillation. *Monthly Weather Review*, 133, 3579–3594.

Barnes, H.C. & Houze, R.A. (2013) The precipitating cloud population of the Madden-Julian oscillation over the Indian and West Pacific oceans. *Journal of Geophysical Research – Atmospheres*, 118, 6996–7023. Available from: https://doi.org/10.1002/jgrd.50375

Bessho, K., Date, K., Hayashi, M., Ikeda, A., Imai, T., Inoue, H. et al. (2016) An introduction to Himawari-8/9–Japan's new-generation geostationary meteorological satellites. *Journal of the Meteorological Society of Japan*, 94, 151–183.

Birch, C.E., Webster, S., Peatman, S.C., Parker, D.J., Matthews, A.J., Li, Y. et al. (2016) Scale interactions between the MJO and the Western Maritime Continent. *Journal of Climate*, 29, 2471–2492.

Bouniol, D., Roca, R., Fiolleau, T. & Raberanto, P. (2021) Life cycle–resolved observation of radiative properties of mesoscale convective systems. *Journal of Applied Meteorology and Climatology*, 60, 1091–1104. Available from: https://doi.org/10.1175/JAMC-D-20-0244.1

Chang, C. (1970) Westward propagating cloud patterns in the tropical Pacific as seen from time-composite satellite photographs. *Journal of the Atmospheric Sciences*, 27(1), 133–138. Available from: https://doi.org/10.1175/1520-0469(1970)027<0133:WPCPIT>2.0.CO;2

Chen, W.-T., Hsu, S.-P., Tsai, W. & Sui, C.-H. (2019) The influences of convectively-coupled Kelvin waves on multi-scale rainfall variability over South China Sea and Maritime Continent in December 2016. *Journal of Climate*, 32, 6977–6993. Available from: https://doi.org/10.1175/JCLI-D-18-0471.1

Cheng, Y.-M., Dias, J., Kiladis, G., Feng, Z. & Leung, L.R. (2023) Mesoscale convective systems modulated by convectively coupled equatorial waves. *Geophysical Research Letters*, 50, e2023GL103335. Available from: https://doi.org/10.1029/2023GL103335

Coppin, D., Bellon, G., Pletzer, A. & Scott, C. (2020) Detecting and tracking coastal precipitation in the tropics: methods and insights into multiscale variability of tropical precipitation. *Journal of Climate*, 33, 6689–6705.

Crook, J., Klein, C., Folwell, S., Taylor, C.M., Parker, D.J., Stratton, R. et al. (2019) Assessment of the representation of west African storm lifecycles in convection-permitting simulations. *Earth and Space Science*, 6, 818–835. Available from: https://doi.org/10.1029/2018EA000491

Da Silva, N.A. & Matthews, A.J. (2021) Impact of the Madden–Julian oscillation on extreme precipitation over the Western Maritime Continent and Southeast Asia. *Quarterly Journal of the Royal Meteorological Society*, 147, 3434–3453.

Da Silva, N.A., Webber, B.G., Matthews, A.J., Feist, M.M., Stein, T.H., Holloway, C.E. et al. (2021) Validation of GPM IMERG extreme precipitation in the maritime continent by station and radar data. *Earth and Space Science*, 8(7), e2021EA001738. Available from: https://doi.org/10.1029/2021EA001738

Del Genio, A.D., Chen, Y.-H., Kim, D. & Yao, M.-S. (2012) The MJO transition from shallow to deep convection in CloudSat/CALIPSO data and GISS GCM simulations. *Journal of Climate*, 25, 3755–3770. Available from: https://doi.org/10.1175/JCLI-D-11-00384.1

DeMott, C.A., Wolding, B.O., Maloney, E.D. & Randall, D.A. (2018) Atmospheric mechanisms for MJO decay over the maritime continent. *Journal of Geophysical Research: Atmospheres*, 123, 5188–5204. Available from: https://doi.org/10.1029/2017JD026979

Dickinson, M. & Molinari, J. (2002) Mixed Rossby–gravity waves and Western Pacific tropical cyclogenesis. Part I: synoptic evolution. *Journal of the Atmospheric Sciences*, 59, 14, 2183–2196. Available from: https://doi.org/10.1175/1520-0469(2002)059<2183:MRGWAW>2.0.CO;2

Feng, X., Yang, G.-Y., Hodges, K.I. & Methven, J. (2023) Equatorial waves as useful precursors to tropical cyclone occurrence and intensification. *Nature Communications*, 14, 511. Available from: https://doi.org/10.1038/s41467-023-36055-5

Feng, Z., Leung, L.R., Liu, N., Wang, J., Houze, R.A., Li, J. et al. (2021) A global high-resolution mesoscale convective system database using satellite-derived cloud tops, surface precipitation, and tracking. *Journal of Geophysical Research: Atmospheres*, 126, e2020JD034202. Available from: https://doi.org/10.1029/2020JD034202

Ferrett, S., Yang, G.Y., Woolnough, S., Methven, J., Hodges, K. & Holloway, C.E. (2020) Linking extreme precipitation in Southeast Asia to equatorial waves. *Quarterly Journal of the Royal Meteorological Society*, 146, 665–684. Available from: https://doi.org/10.1002/qj.3699

Fiolleau, T. & Roca, R. (2013) An algorithm for the detection and tracking of tropical mesoscale convective systems using infrared images from geostationary satellite. *IEEE Transactions on Geoscience and Remote Sensing*, 51(7), 4302–4315. Available from: https://doi.org/10.1109/TGRS.2012.2227762

Fitzpatrick, R.G.J., Parker, D.J., Marsham, J.H., Rowell, D.P., Guichard, F.M., Taylor, C.M. et al. (2020) What drives the intensification of mesoscale convective systems over the west African Sahel under climate change? *Journal of Climate*, 33, 3151–3172. Available from: https://doi.org/10.1175/JCLI-D-19-0380.1

Frank, W. & Roundy, P. (2006) The role of tropical waves in tropical cyclogenesis. *Monthly Weather Review*, 134(9), 2397–2417. Available from: https://doi.org/10.1175/MWR3204.1

Gill, A.E. (1980) Some simple solutions for heat-induced tropical circulation. *Quarterly Journal of the Royal Meteorological Society*, 106, 447–462. Available from: https://doi.org/10.1002/qj.49710644905

Guo, L., Klingaman, N.P., Vidale, P.L., Turner, A.G., Demory, M.-E. & Cobb, A. (2017) Contribution of tropical cyclones to atmospheric moisture transport and rainfall over East Asia. *Journal of*

Climate, 30, 3853–3865. Available from: https://doi.org/10.1175/JCLI-D-16-0308.1

Hagos, S.M., Zhang, C., Feng, Z., Burleyson, C.D., De Mott, C., Kerns, B. et al. (2016) The impact of the diurnal cycle on the propagation of Madden-Julian oscillation convection across the maritime continent. *Journal of Advances in Modeling Earth Systems*, 8, 1552–1564.

Hendon, H.H. & Liebmann, B. (1994) Organization of convection within the Madden-Julian oscillation. *Journal of Geophysical Research*, 99, 8073–8083.

Hersbach, H., Bell, B., Berrisford, P., Biavati, G., Horányi, A., Muñoz Sabater, J. et al. (2023) ERA5 hourly data on pressure levels from 1940 to present. Copernicus Climate Change Service (C3S) Climate Data Store (CDS). DOI: 10.24381/cds.bd0915c6 [Accessed 3rd April-2023].

Hersbach, H., Bell, B., Berrisford, P., Hirahara, S., Horányi, A., Muñoz-Sabater, J. et al. (2020) The ERA5 global reanalysis. *Quarterly Journal of the Royal Meteorological Society*, 146, 1999–2049. Available from: https://doi.org/10.1002/qj.3803

Houze, R.A. (1997) Stratiform precipitation in regions of convection: a meteorological paradox? *Bulletin of the American Meteorological Society*, 78, 2179–2196.

Houze, R.A. (2004) Mesoscale convective systems. *Reviews of Geophysics*, 42, 43.

Houze, R.A. (2018) 100 years of research on mesoscale convective systems. *Meteorological Monographs*, 59, 17.1–17.54. Available from: https://doi.org/10.1175/AMSMONOGRAPHS-D-18-0001.1

Hsu, L., Tseng, L., Hou, S., Chen, B. & Sui, C. (2020) A simulation study of kelvin waves interacting with synoptic events during December 2016 in the South China Sea and maritime continent. *Journal of Climate*, 33(15), 6345–6359. Available from: https://doi.org/10.1175/JCLI-D-20-0121.1

Huang, P., Chou, C. & Huang, R. (2012) The activity of convectively coupled equatorial waves in CMIP3 global climate models. *Theoretical and Applied Climatology*, 112(3–4), 697–711. Available from: https://doi.org/10.1007/s00704-012-0761-4

Huang, X., Hu, C., Huang, X., Chu, Y., Tseng, Y.H., Zhang, G.J. et al. (2018) A long-term tropical mesoscale convective systems dataset based on a novel objective automatic tracking algorithm. *Climate Dynamics*, 51(7–8), 3145–3159. Available from: https://doi.org/10.1007/s00382-018-4071-0

Huffman, G.J., Bolvin, D.T., Nelkin, E.J. & Tan, J. (2020) Integrated Multi-satellitE Retrievals for GPM (IMERG) Technical Documentation. https://docserver.gesdisc.eosdis.nasa.gov/public/project/GPM/IMERG_doc.06.pdf [accessed 16th March 2022]

Jeong, J.-H., Kim, B.-M., Ho, C.-H. & Noh, Y.-H. (2008) Systematic variation in wintertime precipitation in East Asia by MJO-induced extratropical vertical motion. *Journal of Climate*, 21, 788–801.

Jones, C., Waliser, D.E., Lau, K.M. & Stern, W. (2004) Global occurrences of extreme precipitation and the Madden-Julian oscillation: observations and predictability. *Journal of Climate*, 17, 4575–4589.

Kiladis, G.N., Wheeler, M.C., Haertel, P.T., Straub, K.H. & Roundy, P.E. (2009) Convectively coupled equatorial waves. *Reviews of Geophysics*, 47(2), RG2003. Available from: https://doi.org/10.1029/2008RG000266

Klein, C., Belušić, D. & Taylor, C.M. (2018) Wavelet scale analysis of mesoscale convective systems for detecting deep convection from infrared imagery. *Journal of Geophysical Research: Atmospheres*, 123(6), 3035–3050. Available from: https://doi.org/10.1002/2017JD027432

Knapp, K.R., Kruk, M.C., Levinson, D.H., Diamond, H.J. & Neumann, C.J. (2010) The international best track archive for climate stewardship (IBTrACS): unifying tropical cyclone data. *Bulletin of the American Meteorological Society*, 91(3), 363–376. Available from: https://doi.org/10.1175/2009BAMS2755.1

Knippertz, P., Gehne, M., Kiladis, G.N., Kikuchi, K., Satheesh, A.R., Roundy, P.E. et al. (2022) The intricacies of identifying equatorial waves. *Quarterly Journal of the Royal Meteorological Society*, 148, 2814–2852. Available from: https://doi.org/10.1002/qj.4338

Lafore, J.P., Chapelon, N., Diop, M., Gueye, B., Largeron, Y., Lepape, S. et al. (2017) Deep convection. In: Parker, D.J. & Diop-Kane, M. (Eds.) *Meteorology of tropical West Africa: the Forecasters' handbook*. Chichester, UK: John Wiley & Sons, Ltd, pp. 90–129.

Laing, A.G. & Fritsch, J.M. (1997) The global population of mesoscale convective complexes. *Quarterly Journal of the Royal Meteorological Society*, 123(538), 389–405. Available from: https://doi.org/10.1002/qj.49712353807

Latos, B., Lefort, T., Flatau, M.K., Flatau, P.J., Permana, D.S., Baranowski, D.B. et al. (2021) Equatorial waves triggering extreme rainfall and floods in Southwest Sulawesi, Indonesia. *Monthly Weather Review*, 149(5), 1381–1401. Available from: https://doi.org/10.1175/MWR-D-20-0262.1

Li, Y. & Stechmann, S.N. (2020) Predictability of tropical rainfall and waves: estimates from observational data. *Quarterly Journal of the Royal Meteorological Society*, 146, 1668–1684. Available from: https://doi.org/10.1002/qj.3759

Liebmann, B. & Hendon, H.H. (1990) Synoptic scale disturbances near the equator. *Journal of the Atmospheric Sciences*, 47, 1463–1479.

Liu, C.T. & Zipser, E. (2013) Regional variation of morphology of organized convection in the tropics and subtropics. *Journal of Geophysical Research: Atmospheres*, 118(2), 453–466. Available from: https://doi.org/10.1029/2012JD018409

Lubis, S.W. & Jacobi, C. (2015) The modulating influence of convectively coupled equatorial waves (CCEWs) on the variability of tropical precipitation. *International Journal of Climatology*, 35, 1465–1483. Available from: https://doi.org/10.1002/joc.4069

Lubis, S.W. & Respati, M.R. (2021) Impacts of convectively coupled equatorial waves on rainfall extremes in Java, Indonesia. *International Journal of Climatology*, 2021(41), 2418–2440. Available from: https://doi.org/10.1002/joc.6967

Madden, R.A. (1986) Seasonal variations of the 40-50 day oscillation in the tropics. *Journal of the Atmospheric Sciences*, 43, 3138–3158.

Madden, R.A. & Julian, P.R. (1971) Detection of a 40-50 day oscillation in the zonal wind in the tropical Pacific. *Journal of the Atmospheric Sciences*, 28, 702–708.

Madden, R.A. & Julian, P.R. (1972) Description of global-scale circulation cells in the tropics with a 40-50 day period. *Journal of the Atmospheric Sciences*, 29, 1109–1123.

Madden, R.A. & Julian, P.R. (1994) Observations of the 40-50 day tropical oscillation–a review. *Monthly Weather Review*, 112, 814–837.

Mapes, B., Tulich, S., Lin, J. & Zuidema, P. (2006) The mesoscale convection life cycle: building block or prototype for large-scale tropical waves? *Dynamics of Atmospheres and Oceans*, 42(1–4), 3–29.

Mathon, V. & Laurent, H. (2001) Life cycle of Sahelian mesoscale convective cloud 765 systems. *Quarterly Journal of the Royal Meteorological Society*, 127, 377–406.

Muhammad, F.R., Lubis, S.W. & Setiawan, S. (2020) Impacts of the Madden-Julian oscillation on precipitation extremes in Indonesia. *International Journal of Climatology*, 41, 1970–1984.

Nakamura, Y. & Takayabu, Y.N. (2022) Convective couplings with equatorial Rossby waves and equatorial kelvin waves. Part II: coupled precipitation characteristics. *Journal of the Atmospheric Sciences*, 79, 2919–2933.

Neale, R. & Slingo, J.M. (2003) The maritime continent and its role in the global climate: a GCM study. *Journal of Climate*, 16, 834–848.

Nesbitt, S.W., Cifelli, R. & Rutledge, S.A. (2006) Storm morphology and rainfall characteristics of TRMM precipitation features. *Monthly Weather Review*, 134, 2702–2721. Available from: https://doi.org/10.1175/MWR3200.1

Oh, J.H., Kim, K.Y. & Lim, G.H. (2012) Impact of MJO on the diurnal cycle of rainfall over the western maritime continent in the austral summer. *Climate Dynamics*, 38, 1167–1180. Available from: https://doi.org/10.1007/s00382-011-1237-4

Peatman, S.C., Klingaman, N.P. & Hodges, K.I. (2019) Tropical cyclone-related precipitation over the northwest tropical Pacific in met Office global operational forecasts. *Weather and Forecasting.*, 34(4), 923–941.

Peatman, S.C., Matthews, A.J. & Stevens, D.P. (2014) Propagation of the Madden-Julian oscillation through the maritime continent and scale interaction with the diurnal cycle of precipitation. *Quarterly Journal of the Royal Meteorological Society*, 140, 814–825.

Peatman, S.C., Schwendike, J., Birch, C.E., Marsham, J.H., Matthews, A.J. & Yang, G.-Y. (2021) A local-to-large scale view of maritime continent rainfall: control by ENSO, MJO, and equatorial waves. *Journal of Climate*, 34(22), 8933–8953. Available from: https://doi.org/10.1175/JCLI-D-21-0263.1

Ramage, C.S. (1968) Role of a tropical "maritime continent" in the atmospheric circulation. *Monthly Weather Review*, 96, 365–370. Available from: https://doi.org/10.1175/1520-0493(1968)096<0365:ROATMC>2.0.CO;2

Roca, R., Aublanc, J., Chambon, P., Fiolleau, T. & Viltard, N. (2014) Robust observational quantification of the contribution of mesoscale convective systems to rainfall in the tropics. *Journal of Climate*, 27(13), 4952–4958. Available from: https://doi.org/10.1175/JCLI-D-13-00628.1

Roca, R. & Ramanathan, V. (2000) Scale dependence of monsoonal convective systems over the Indian Ocean. *Journal of Climate*, 13(7), 1286–1298.

Rotunno, R., Klemp, J.B. & Weisman, M.L. (1988) A theory for strong, long-lived squall lines. *Journal of Atmospheric Sciences*, 45(3), 463–485.

Sakaeda, N., Kiladis, G. & Dias, J. (2020) The diurnal cycle of rainfall and the convectively coupled equatorial waves over the maritime continent. *Journal of Climate*, 33(8), 3307–3331. Available from: https://doi.org/10.1175/JCLI-D-19-0043.1

Schumacher, C. & Houze, R.A. (2003) Stratiform rain in the tropics as seen by the TRMM precipitation radar. *Journal of Climate*, 16, 1739–1756.

Simpson, J., Keenan, T.D., Ferrier, B., Simpson, R.H. & Holland, G.J. (1993) Cumulus mergers in the maritime continent region. *Meteorology and Atmospheric Physics*, 51, 73–99. Available from: https://doi.org/10.1007/BF01080881

Stein, T.H.M., Hogan, R.J., Clark, P., Halliwell, C., Hanley, K., Lean, H. et al. (2015) The DYMECS project: a statistical approach for the evaluation of convective storms in high-resolution NWP models. *Bulletin of the American Meteorological Society*, 96, 939–951.

Stephens, G.L., Webster, P.J., Johnson, R.H., Engelen, R. & L'ecuyer, T. (2004) Observational evidence for the mutual regulation of the tropical hydrological cycle and tropical sea surface temperatures. *Journal of Climate*, 17, 2213–2224.

Takayabu, Y.N. (1994) Large-scale cloud disturbances associated with equatorial waves. Part I: spectral features of the cloud disturbances. *Journal of the Meteorological Society of Japan*, 72, 433–449.

Taylor, C.M., Belušić, D., Guichard, F., Parker, D.J., Vischel, T., Bock, O. et al. (2017) Frequency of extreme Sahelian storms tripled since 1982 in satellite observations. *Nature*, 544, 475–478.

Virtz, K.S. & Houze, R.A. (2015) Variation of lightning and convective rain fraction in mesoscale convective systems of the MJO. *Journal of the Atmospheric Sciences*, 72, 1932–1944. Available from: https://doi.org/10.1175/JAS-D-14-0201.1

Wang, B. & Rui, H. (1990) Synoptic climatology of transient tropical intraseasonal convection anomalies: 1975-1985. *Meteorology and Atmospheric Physics*, 44, 43–61.

Welch, B.L. (1947) The generalization of "Student's" problem when several different population variances are involved. *Biometrika*, 34(1–2), 28–35. Available from: https://doi.org/10.1093/biomet/34.1-2.28

Wheeler, M. & Kiladis, G.N. (1999) Convectively coupled equatorial waves: analysis of clouds and temperature in the wave-number-frequency domain. *Journal of the Atmospheric Sciences*, 56, 374–399.

Wheeler, M.C. & Hendon, H.H. (2004) An all-season real-time multivariate MJO index: development of an index for monitoring and prediction. *Monthly Weather Review*, 132, 1917–1932.

Xavier, P., Rahmat, R., Cheong, W.K. & Wallace, E. (2014) Influence of Madden-Julian oscillation on Southeast Asia rainfall extremes: observations and predictability. *Geophysical Research Letters*, 41, 4406–4412. Available from: https://doi.org/10.1002/2014GL060241

Yanai, M. & Murakami, M. (1970) Spectrum analysis of symmetric and antisymmetric equatorial waves. *Journal of the Meteorological Society of Japan. Ser. II*, 48(4), 331–347. Available from: https://doi.org/10.2151/jmsj1965.48.4_331

Yang, G.-Y., Feng, X. & Hodges, K. (2023) Seasonal and interannual variation of equatorial waves in ERA5 and GloSea5. *Quarterly Journal of the Royal Meteorological Society*, 149(752), 1109–1134. Available from: https://doi.org/10.1002/qj.4460

Yang, G.-Y., Ferrett, S., Woolnough, S., Methven, J. & Holloway, C. (2021) Real-time identification of equatorial waves and evaluation of waves in global forecasts. *Weather and Forecasting*, 36(1), 171–193. Available from: https://doi.org/10.1175/WAF-D-20-0144.1

Yang, G.-Y., Hoskins, B. & Slingo, J. (2003) Convectively coupled equatorial waves: a new methodology for identifying wave structures in observational data. *Journal of the Atmospheric Sciences*, 60, 1637–1654. Available from: https://doi.org/10.1175/1520-0469%282003%29060%3C1637%3ACCEWAN%3E2.0.CO%3B2

Yang, G.-Y., Hoskins, B.J. & Slingo, J.M. (2007a) Convectively coupled equatorial waves. Part I: horizontal structure. *Journal of the Atmospheric Sciences*, 64, 3406–3423.

Yang, G.-Y., Hoskins, B.J. & Slingo, J.M. (2007b) Convectively coupled equatorial waves. Part II: zonal propagation. *Journal of the Atmospheric Sciences*, 64, 3424–3437.

Yang, G.-Y., Hoskins, B.J. & Slingo, J.M. (2007c) Convectively coupled equatorial waves. Part III: synthesis structures and their forcing and evolution. *Journal of the Atmospheric Sciences*, 64, 3438–3451. Available from: https://doi.org/10.1175/JAS4019.1

Yang, G.-Y., Slingo, J. & Hoskins, B. (2009) Convectively coupled equatorial waves in high-resolution Hadley Centre climate models. *Journal of climate*, 22(8), 1897–1919. Available from: https://doi.org/10.1175/2008JCLI2630.1

Yang, Q., Houze, R.A., Leung, L.R. & Feng, Z. (2017) Environments of long-lived mesoscale convective systems over the central United States in convection permitting climate simulations. *Journal of Geophysical Research: Atmospheres*, 122(24), 13288–13307. Available from: https://doi.org/10.1002/2017jd027033

Ying, Y. & Zhang, F. (2017) Practical and intrinsic predictability of multiscale weather and convectively coupled equatorial waves during the active phase of an MJO. *Journal of the Atmospheric Sciences*, 74(11), 3771–3785. Available from: https://doi.org/10.1175/JAS-D-17-0157.1

Yoneyama, K. & Zhang, C. (2020) Years of the maritime continent. *Geophysical Research Letters*, 47, e2020GL087182. Available from: https://doi.org/10.1029/2020GL087182

Yuan, J. & Houze, R.A. (2010) Global variability of mesoscale convective system anvil structure from A-train satellite data. *Journal of Climate*, 23(21), 5864–5888. Available from: https://doi.org/10.1175/2010JCLI3671.1

Yuan, J. & Houze, R.A. (2013) Deep convective systems observed by A-train in the tropical Indo-Pacific region affected by the MJO. *Journal of the Atmospheric Sciences*, 70, 465–486. Available from: https://doi.org/10.1175/JAS-D-12-057.1

Zhang, C. & Dong, M. (2004) Seasonality in the Madden–Julian oscillation. *Journal of Climate*, 17(16), 3169–3180. Available from: https://doi.org/10.1175/1520-0442(2004)017<3169:sitmo>2.0.co;2

Zuluaga, M.D. & Houze, R.A. (2013) Evolution of the population of precipitating cloud systems over the equatorial Indian Ocean in active phases of the Madden–Julian oscillation. *Journal of the Atmospheric Sciences*, 70, 2713–2725. Available from: https://doi.org/10.1175/JAS-D-12-0311.1

SUPPORTING INFORMATION

Additional supporting information can be found online in the Supporting Information section at the end of this article.

How to cite this article: Crook, J., Morris, F., Fitzpatrick, R.G.J., Peatman, S.C., Schwendike, J., Stein, T.H. *et al.* (2024) Impact of the Madden–Julian oscillation and equatorial waves on tracked mesoscale convective systems over southeast Asia. *Quarterly Journal of the Royal Meteorological Society*, 150(760), 1724–1751. Available from: https://doi.org/10.1002/qj.4667